RSC Sustainability

ROYAL SOCIETY OF CHEMISTRY

PAPER

View Article Online
View Journal | View Issue

Cite this: *RSC Sustainability*, 2025, **3**, 4137

An Fe_3O_4@keratin nanocomposite doped with copper(II): a reusable heterogeneous catalyst for the synthesis of novel 1,4-disubstituted 1,2,3-triazole-pyrimido-benzimidazoles in aqueous ethanolic solution under ultrasound cavitation†

Chaimae Hourma,[a] Mohamed Belhajja,[a] Mohsine Driowya,[ab] Hamza Tachallait,[c] Rachid Benhida[cd] and Khalid Bougrin *[ac]

Received 2nd May 2025
Accepted 21st July 2025

DOI: 10.1039/d5su00318k

rsc.li/rscsus

A novel magnetic nanocatalyst, Fe_3O_4@keratin-Cu(II), was developed *via* simple aqueous-phase immobilization of Cu(II) onto a keratin-coated Fe_3O_4 surface, with keratin extracted from chicken feathers through ultrasonic-assisted alkaline-oxidative hydrolysis. This catalyst enabled a rapid and green sequential two-step, one-pot synthesis of 1,2,3-triazolo-pyrimido-benzimidazole derivatives **5a–x** in good to excellent yields (64–90%). The protocol involves microwave-assisted propargylation of benzimidazo[1,2-*a*]pyrimidinone followed by a CuAAC "click" reaction with azides under ultrasonic cavitation. The Fe_3O_4@KNPs-Cu(II) nanocatalyst showed very high activity for the click reaction and demonstrated excellent recyclability over five cycles without loss of activity. The structures of the nanocomposite and products **5a–x** were fully characterized using FT-IR, XRD, SEM-EDX, ICP-OES, AFM, TEM, HRTEM, TGA, DSC, ^{1}H NMR, ^{13}C NMR, ^{19}F NMR, and HRMS techniques. The use of ultrasound significantly enhanced the reaction rate, offering a clean and efficient synthetic route.

Sustainability spotlight

This work contributes to green chemistry by valorizing biomass, specifically keratin extracted from chicken feathers, to develop a novel, reusable, heterogeneous and magnetic nanocatalyst [Fe_3O_4@KNPs-Cu(II)]. The nanocomposite enables an efficient, eco-friendly sequential one-pot two-step (propargylation/CuAAC) synthesis of triazolo-pyrimido-benzimidazole derivatives **5a–x** in aqueous ethanol under ultrasonic cavitation. This approach replaces traditional multistep protocols that rely on toxic solvents, free Cu(II) salts and non-recyclable catalysts. The developed procedure demonstrated significant improvements in green chemistry standards. A 36-fold rate enhancement compared to conventional CuAAC was achieved, affording products **5a–x** in 64–90% yields within 20–120 minutes under mild conditions. The process uses only 10 wt% catalyst, which was easily recovered and reused over five consecutive cycles without significant loss of its catalytic performance. Our work aligns with several prioritized United Nations Sustainable Development Goals (SDGs), including SDG 12: responsible consumption and production: by valorizing chicken feather waste (a biomass byproduct) into keratin and developing a recyclable, heterogeneous nanocatalyst, the research promotes sustainable material use and waste minimization; SDG 9: industry, innovation and infrastructure: through the development of a novel magnetic nanocatalyst and green synthetic methods (microwave and ultrasound-assisted), the work advances innovation in sustainable chemical processes and catalytic technologies; SDG 13: climate action: by applying green chemistry principles (solvent-free conditions, energy-efficient activation, and recyclable catalysts), the work reduces the environmental footprint and supports efforts toward climate change mitigation and SDG 3: good health and well-being (potentially, depending on the bioactivity of the synthesized compounds): if the 1,2,3-triazolo-pyrimido-benzimidazole derivatives are intended for pharmaceutical or biomedical applications, they could contribute to the development of new therapeutic agents.

Introduction

The advent of benign conditions in heterocyclic synthesis represents a crucial stride toward a more sustainable future, where the exploration of aza-heterocycles converges with the imperative to mitigate the environmental impact of chemical processes.[1–3] This approach involves a judicious selection of reagents,[4] solvents,[5] catalysts[6] and activation methods.[7] Particularly, the development of eco-friendly recyclable catalysts, including the implementation of heterogeneous catalysis has

[a]*Equipe de Chimie des Plantes et de Synthèse Organique et Bioorganique, URAC23, Faculty of Science, Geophysics, Natural Patrimony and Green Chemistry (GEOPAC) Research Center, Mohammed V University in Rabat, B.P. 1014, Morocco. E-mail: k.bougrin@um5r.ac.ma*

[b]*Higher School of Technology, Sultan Moulay Slimane University, B.P. 170, Khenifra, 54006, Morocco*

[c]*Chemical & Biochemical Sciences – Green Process Engineering (CBS) Mohammed VI Polytechnic University, Lot 660, Hay Moulay Rachid, Benguerir, 43150, Morocco*

[d]*Université Côte d'Azur, CNRS, Institut de Chimie de Nice, UMR CNRS 7272, Nice, 06108, France*

† Electronic supplementary information (ESI) available. See DOI: https://doi.org/10.1039/d5su00318k

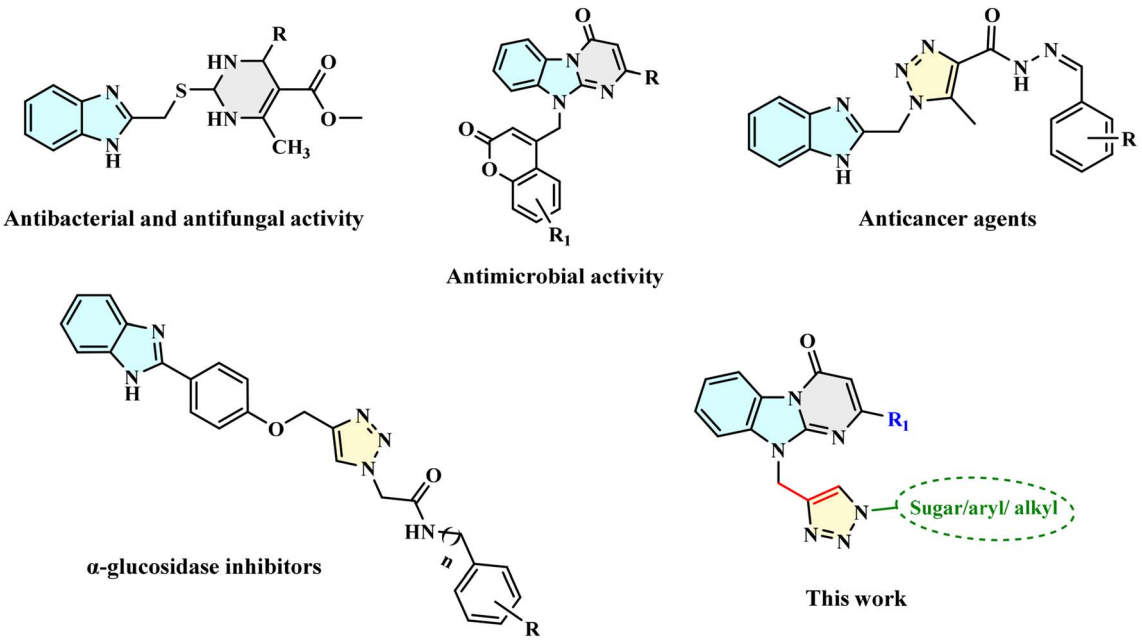

Fig. 1 Bioactive hybrid compounds containing pyrimidine, benzimidazole or 2-aminobenzimidazole and 1,2,3-triazole.

become a major challenge in current chemical research contrasting with conventional catalytic approaches.[8] Various catalytic applications have seen the successful deployment of a diverse array of solid-supported catalysts, from traditional heterogeneous systems like palladium on carbon (Pd/C)[9] to advanced materials such as metal–organic frameworks (MOFs).[10,11] These catalysts have demonstrated significant potential in heterocyclic synthesis offering enhanced efficiency, selectivity and sustainability in the construction of complex heterocyclic compounds.[12,13] Despite the numerous advantages associated with solid-supported catalysts, they are not exempt from challenges with the implementation of effective solutions. These challenges often involve a combination of innovative material design with high cost of catalyst materials, advanced synthesis techniques, potential catalyst leaching and issues of catalyst toxicity in addition to a deeper understanding of the underlying catalytic mechanisms on solid supports.[14–16] In this context, the combination of nanotechnology and biopolymer chemistry has opened new avenues for developing novel catalyst supports that offer intrinsic biocompatibility and low toxicity.[17] This innovative approach encompasses natural biopolymers such as chitin/chitosan,[18] collagen,[19] cellulose,[20] starch,[21] pectin,[22] lignin,[23] and alginate,[24] which serve as exemplary matrices for the immobilization of transition metal nanocatalyst species, including copper,[25] silver,[26] zinc[27] and iron.[28]

Over the past few decades, the chemistry of aza-heterocycles has received considerable attention due to the wide spectrum of their biological activity and numerous therapeutic applications in medicine.[29] In the field of drug discovery, 1,2,3-triazole, pyrimidine, benzimidazole or 2-aminobenzimidazole are heterocycles well known for their significant therapeutic and medicinal properties.[30] The combination of these biologically active motifs in a single molecule known as a hybrid has been of great interest statement in medicinal chemistry thanks to their antimicrobial,[31] antibacterial and antifungal properties,[32] in addition to their activity as anticancer agents[33] and α-glucosidase inhibitors[34] (Fig. 1). Even though they hold great biological significance, their synthesis has been scarcely reported in the literature.

Over the last few years, the 1,3-dipolar cycloaddition (1,3-DC) of azide with alkyne has been ameliorated by the use of copper(I) (CuAAC), and widely applied for the regioselective synthesis of 1,4-disubstituted 1,2,3-triazoles.[35–37] This groundbreaking work was recognized with the Nobel Prize in Chemistry three years ago.[38] However, CuAAC protocols face significant challenges primarily due to the homogeneous nature of the catalysts which complicate the separation process of the catalyst from the final product.[39] Moreover, the protocols often necessitate the inclusion of significant stoichiometric amounts of Cu(I) or catalytic quantities of Cu(II) in the presence of stabilizing ligands and reducing agents (*e.g.* sodium ascorbate), related to redox processes of Cu(I)/Cu(II) species under aerobic conditions and its thermodynamic instability.[40] This can promote parasitic reactions like Glaser coupling.[41a] In addition, the problem of chelation of Cu(I) and Cu(II) by several heterocycles containing nitrogen atoms prevents or complicates access to these compounds.[41b,c] Consequently, developing efficient heterogeneous systems is highly desirable to overcome these disadvantages.[42] Numerous recent studies have underscored the importance of employing heterogeneous catalytic conditions based on biopolymers in the synthesis of 1,2,3-triazoles.[25] Notably, the immobilization of Cu(I) and Cu(II) on biopolymers such as chitin,[25a] chitosan,[25b] starch,[25c] alginate,[25d] cellulose,[25e] and pectin[25f] was used in click synthesis. This approach leads to higher yields of desired products with fewer by-products,[43] simple separation of the catalyst and products by

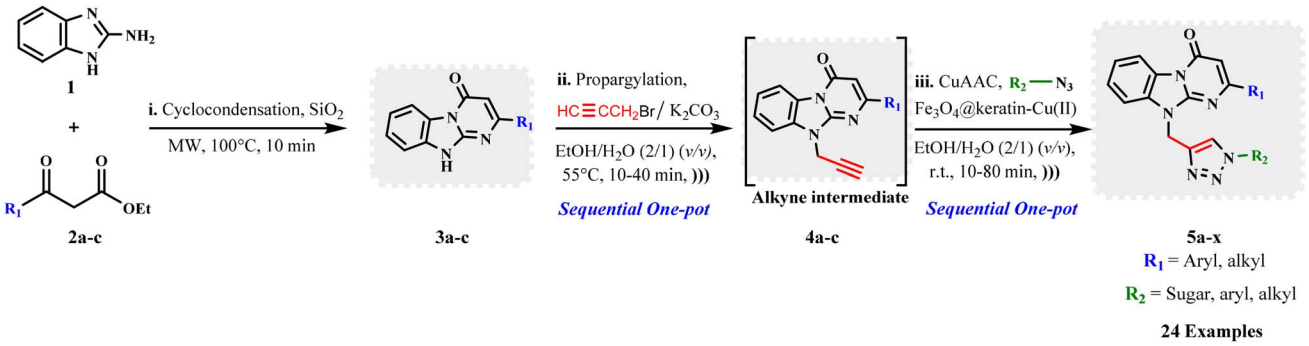

Scheme 1 Synthesis strategy of new fused pyrimido-benzimidazole-based 1,2,3-triazole derivatives **5a–x** under microwave and ultrasound irradiation.

a filtration or centrifugation process from the reaction mixture and reusability of the catalyst resulting in longer catalyst lifetimes.[44] In this context, magnetically separable nanocomposites emerge as a promising solution, and this synergy fosters greener and more sustainable synthetic routes.[45] Therefore, keratin is considered one of the most natural important biopolymers, it can be used as a matrix and obtained from various biomass sources like feathers, hair, wool, animal claws, and fingernails,[46] and extracted using straightforward techniques.[47] Moreover, its biodegradable properties and its protein structure containing a different sequence of amino acids provides ample bonding sites for catalyst incorporation, minimizing the need for complex processes and costly resources.[48] This opens new paths for eco-friendly synthetic approaches. To the best of our knowledge, keratin has not been previously reported as a nanocomposite material for the synthesis of new heterocyclic compounds. Additionally, the use of green solvents is imperative to mitigate contamination issues caused by catalysts.[49]

On the other hand, one-pot multi-step processes have gained significant attention in heterocyclic synthesis owing to their many benefits.[50,51] As a result, it often leads to shorter reaction durations and lower energy consumption making it a more sustainable and practical strategy.[52] Similarly, ultrasound-assisted synthesis of inorganic and organic materials has drawn considerable interest for its compatibility with green chemistry.[53,54] Numerous studies have explored the integration of nanocomposites with ultrasonic cavitation to facilitate the synthesis of valuable nitrogen-containing heterocyclic compounds.[55]

In this regard, our research team has previously conducted several studies on the effect of ultrasound on the design of new aza-heterocycles,[56] highlighting the contribution of this technique in enhancing the reaction efficiency in heterogeneous systems.[57,58]

In light of the above discussions, we describe for the first time a novel and efficient method for synthesis of new fused pyrimido-benzimidazole-based 1,2,3-triazole derivatives **5a–x** under ultrasonic cavitation in aqueous ethanol using the newly prepared magnetic Fe_3O_4@KNPs nanocomposite (KNPs: keratin nanoparticles) coated with copper(II) as an eco-friendly catalyst (Scheme 1).

Results and discussion

We began our investigations by the preparation of new magnetic Fe_3O_4@KNPs coated with copper(II), which will serve as a catalyst in a subsequent step as described below.

Synthesis and characterization of the Fe_3O_4@KNPs-Cu(II) catalyst

To synthesize the Fe_3O_4@KNPs-Cu(II) nanocatalyst, a homogeneous solution of soluble keratin was obtained by alkaline oxidation, followed by the dropwise addition of 1 M HCl solution to precipitate keratin. The shear stress generated by ultrasonic waves was used to assist the generation of KNPs (Fig. 2a).[59] The process of forming Fe_3O_4 within the network of KNPs initiates with the attraction of Fe^{2+} and Fe^{3+} ions towards the functional groups of KNPs.[60] Subsequently, upon the addition of NH_4OH into the system, the OH groups interact with the Fe^{2+} and Fe^{3+} ions, leading to their hydrolysis and the formation of $Fe(OH)_3$/$Fe(OH)_2$. Following this, through the condensation of $Fe(OH)_3$/$Fe(OH)_2$, the KNPs were chemically grafted onto the Fe_3O_4 nanoparticles (Fig. 2b).[61] Following the successful grafting of KNPs onto the Fe_3O_4 nanoparticles, the resulting Fe_3O_4@KNPs were employed for the adsorption of copper ions. The functional groups of KNPs, particularly the amide (–CONH) groups from amino acids, played a pivotal role in the capture of Cu^{2+} ions through electrostatic interactions and coordination forces (Fig. 2c).[60,62]

The XRD patterns of KNPs, Fe_3O_4@KNPs, and Fe_3O_4@KNPs-Cu(II) are presented in Fig. 3. The KNP diffractogram displays characteristic peaks at 19.0° and 21.1° corresponding to the β-sheet crystalline structure of keratin. For both Fe_3O_4@KNPs and Fe_3O_4@KNPs-Cu(II), distinct diffraction peaks are observed at 2θ = 30.1°, 35.6°, 43.0°, 53.9°, 57.3°, 62.5°, and 74.7°, which are assigned to the (220), (311), (400), (422), (511), (440), and (533) planes of the inverse cubic spinel structure of magnetite Fe_3O_4 (JCPDS Card no. 19-0629). These peaks, while detectable, are moderately broadened, a phenomenon consistent with Fe_3O_4@biopolymer composites, where the amorphous matrix suppresses sharp diffraction signals. The addition of Cu(II) ions does not introduce new crystalline phases; the absence of discrete Cu-related peaks confirms that copper remains

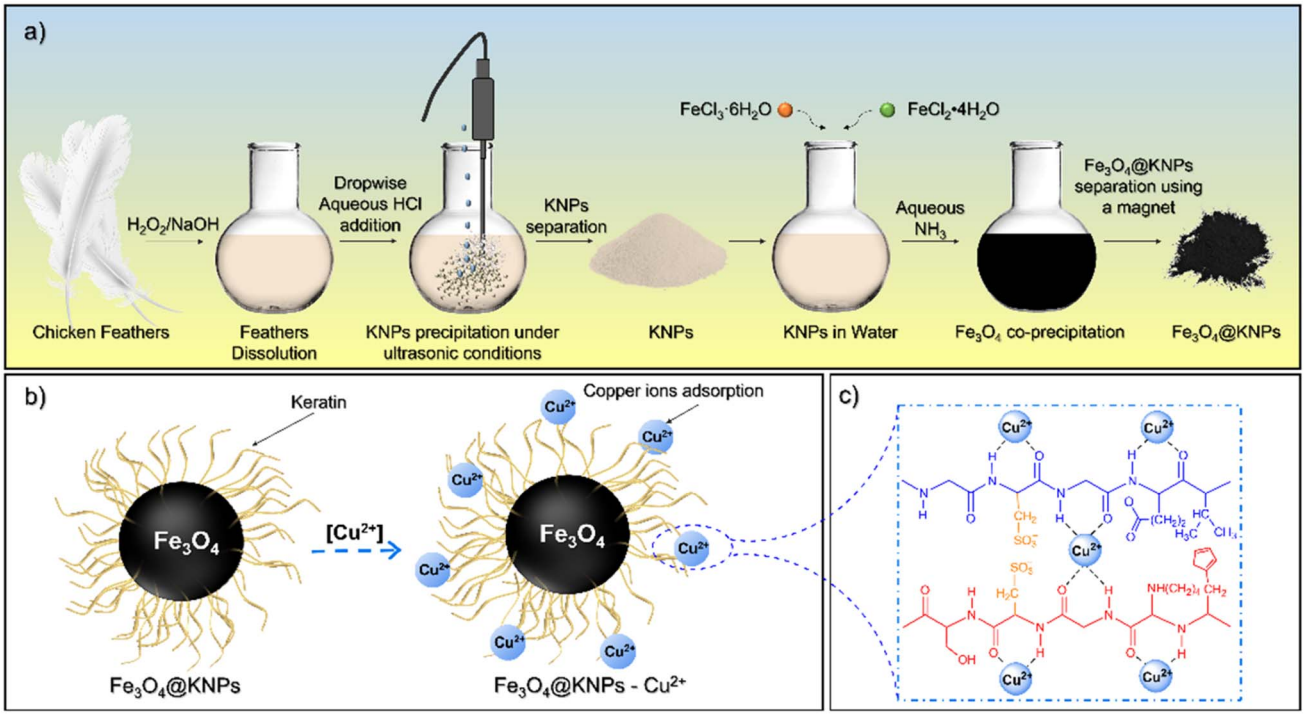

Fig. 2 Schematic representation illustrating (a) the synthesis process of Fe_3O_4@KNPs, (b) the functionalization of KNPs with Fe_3O_4 and subsequent Cu(II) immobilization, and (c) the Cu^{2+} ion adsorption mechanism facilitated by the functional groups of KNPs.

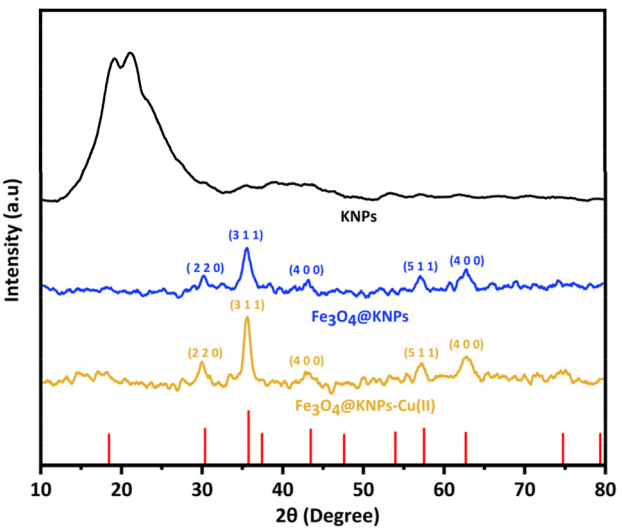

Fig. 3 XRD patterns of KNPs, Fe_3O_4@KNPs, and Fe_3O_4@KNPs-Cu(II).

ionically bound within theFe_3O_4@KNPs matrix, rather than forming separate crystalline copper compounds.

To determine the crystal size, Scherrer's equation (eqn (1)) was employed:

$$D = \frac{K\lambda}{\beta\cos(\theta)} \quad (1)$$

where D represents the crystal size, K is the Scherrer coefficient (0.89), λ is the X-ray wavelength ($\lambda = 0.154056$ nm), θ is the Bragg angle, and β is the full width at half-maximum (FWHM) in radians.

Upon synthesizing Fe_3O_4@KNPs and subsequently adsorbing copper ions onto their surface, a slight decrease in crystallite size from 6.0 nm to 5.1 nm was observed (Table 1). This reduction can be attributed to several interrelated factors. Firstly, the adsorption of copper ions onto the surface of Fe_3O_4 nanoparticles introduces surface stress, leading to lattice distortions and a reduction in crystallite size.[63] Secondly, the incorporation of copper ions can introduce strain and defects into the Fe_3O_4 lattice, further distorting its structure and reducing the coherent diffraction domain size.[64,65] Additionally, the interaction between copper ions and functional groups present in keratin can lead to conformational changes in its matrix, exerting mechanical stress on the embedded Fe_3O_4 nanoparticles and potentially reducing their crystallite size.[66] Lastly, copper adsorption could cause de-aggregation of nanoparticle clusters, breaking larger aggregates into smaller, more dispersed crystallites, which would also contribute to the perceived decrease in crystallite size.[67]

FTIR spectroscopy was employed to analyze the chemical composition of the KNPs and Fe_3O_4@KNPs, and the impact of

Table 1 The crystallite size values obtained using Scherrer's equation

Substance	Most intense peak (2θ, degree)	*hkl*	β (radian)	Crystallite sizes (D, nm)
Fe_3O_4@KNPs	35.6	311	1.4	6.0
Fe_3O_4@KNPs-Cu(II)	35.6	311	1.6	5.1

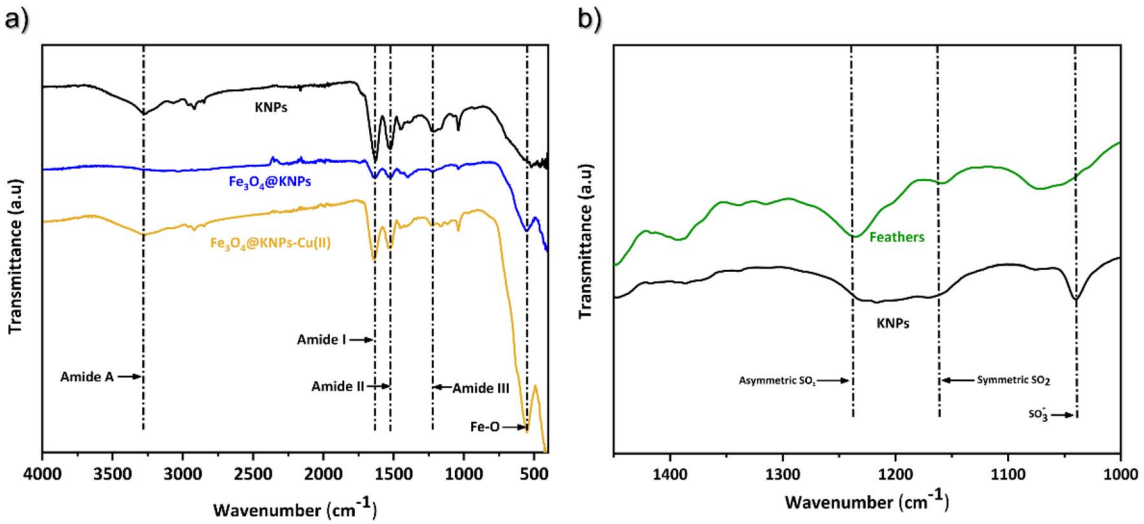

Fig. 4 (a) FTIR spectra of KNPs, Fe_3O_4@KNPs, and the Fe_3O_4@KNPs-Cu(II) nanocatalyst; (b) the S–O fingerprint region in the spectral range of 1450 to 1000 cm^{-1}.

copper adsorption on the chemical structure of the final product (Fig. 4). The broad vibration band region observed between 3675 and 3108 cm^{-1} was attributed to the stretching vibrations of O–H and N–H bonds (amide A).[68] Bands appearing in the range of 3000 to 2825 cm^{-1} were identified as stretching bonds of C–H. The absorption peak associated with amide I, predominantly reflecting C=O stretching, was detected within the range of 1766–1575 cm^{-1}.[69] Amide II, linked to N–H bending and C–H stretching vibrations, exhibited absorption in the range of 1575–1473 cm^{-1}. Additionally, bands observed between 1293 and 1117 cm^{-1} were assigned to the amide III band, resulting from the combination of N–H bending and C–N stretching vibrations.[70] An additional peak at 550 cm^{-1} was observed for the Fe_3O_4@KNPs, corresponding to the stretching of the Fe–O bond. This additional peak signifies the successful incorporation of Fe_3O_4 into the KNPs, further validating the formation of the composite material. Changes in the intensity of specific peak characteristics within the Fe_3O_4@KNPs biosorbent were noticed before and after copper adsorption. A slight increase in intensity was observed, suggesting the involvement of surface functional groups in the adsorption of copper ions.[71] In the context of keratin, particularly rich in disulfide bonds, like cysteine, the oxidation process induces the formation of subsequent species characterized by varying sulfur oxidation states, such as sulfinic ($R–SO_2H$) or sulfonic ($R–SO_3H$) acids.[72] The spectral range spanning from 1450 to 1000 cm^{-1}

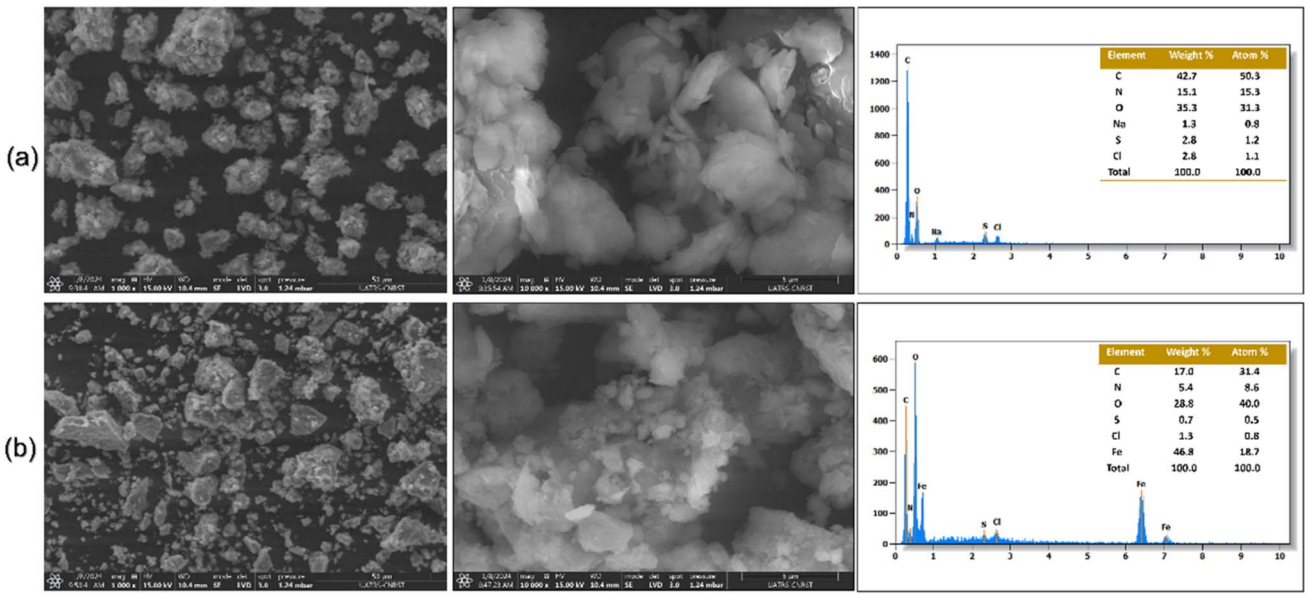

Fig. 5 SEM images at two different magnifications and EDX spectra of (a) KNPs and (b) Fe_3O_4@KNPs.

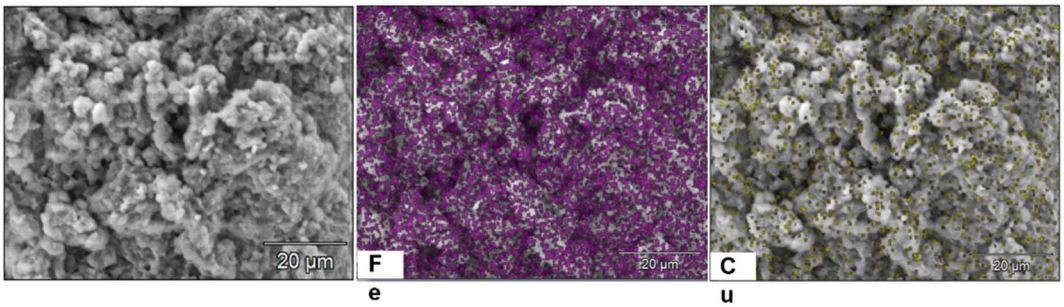

Fig. 6 Fe and Cu elemental mapping images of Fe_3O_4@KNPs-Cu(II).

was meticulously examined to discern variations in the S–O fingerprint FTIR spectrum, as illustrated in Fig. 4b. Notably, distinctive enhancements in the spectra were observed for the regenerated keratin compared to feathers. These enhancements included the intensification of the band at 1041 cm^{-1} attributed to oxidized sulfur derivatives like cysteic acid (K–SO_3H),[73] the symmetric SO_2 band at 1172 cm^{-1}, and the asymmetric SO_2 band at 1235 cm^{-1}, indicative of oxidation and concurrent cleavage of disulfide bonds.[74]

The SEM images obtained during the characterization of our catalyst offer valuable insights into its structural morphology and composition. Prior to the addition of the magnetite material (Fig. 5a), the KNPs exhibit a polygonal irregular-shaped morphology, with one-dimensional nanometric particles forming agglomerated structures interconnected with each other. This morphology suggests a certain degree of compactness and cohesion within the keratin matrix. The EDX spectra shown in (Fig. 5a) confirm the typical elemental composition of keratin, revealing the presence of carbon (C), oxygen (O), and nitrogen (N), alongside sulfur (S), which is characteristic of the amino acids that constitute keratin. Upon the functionalization with the Fe_3O_4 material, significant changes in the surface morphology of the nanocomposite Fe_3O_4@KNPs are observed (Fig. 5b). The SEM images reveal the presence of numerous spherical-like nanoparticles uniformly distributed on and adhering to the surface of the KNPs. This results in the formation of a rougher surface texture compared to that of the pristine KNPs. The EDX spectra in Fig. 5b further confirm the successful deposition of Fe_3O_4, as evidenced by the appearance of iron (Fe) peaks. Additionally, an increase in the percentage of oxygen is observed, indicating the presence of oxidized iron species. These structural modifications hold significant implications for the adsorption process of copper ions and catalytic activities. The rougher surface texture of the Fe_3O_4@KNPs nanocomposite provides a larger surface area and more active sites for the adsorption of copper ions.[75]

The SEM and EDX elemental mapping images (Fig. 6) provide complementary insights into the structural and compositional characteristics of the Fe_3O_4@KNPs-Cu(II) nanocomposite. SEM analysis reveals a rough yet more uniform surface morphology, characterized by rounded features, which suggests a well-dispersed distribution of deposited Fe_3O_4 nanoparticles and adsorbed Cu(II) ions. This observation aligns with the EDX elemental mapping results, which confirm the

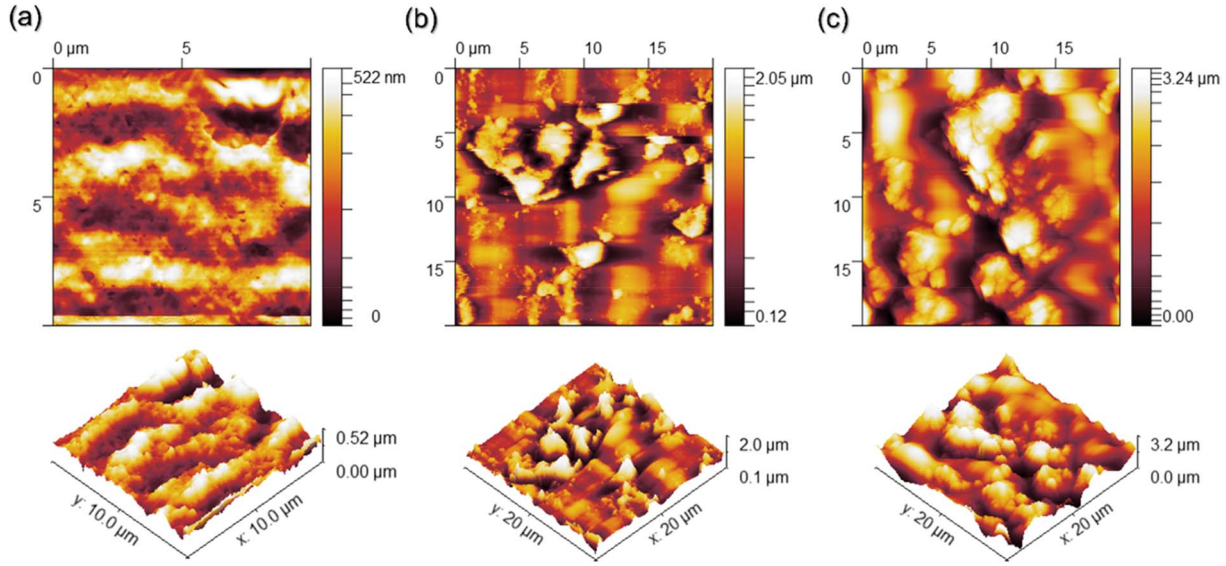

Fig. 7 AFM images of KNPs at different functionalization stages: (a) KNPs, (b) Fe_3O_4@KNPs, and (c) Fe_3O_4@KNPs-Cu(II).

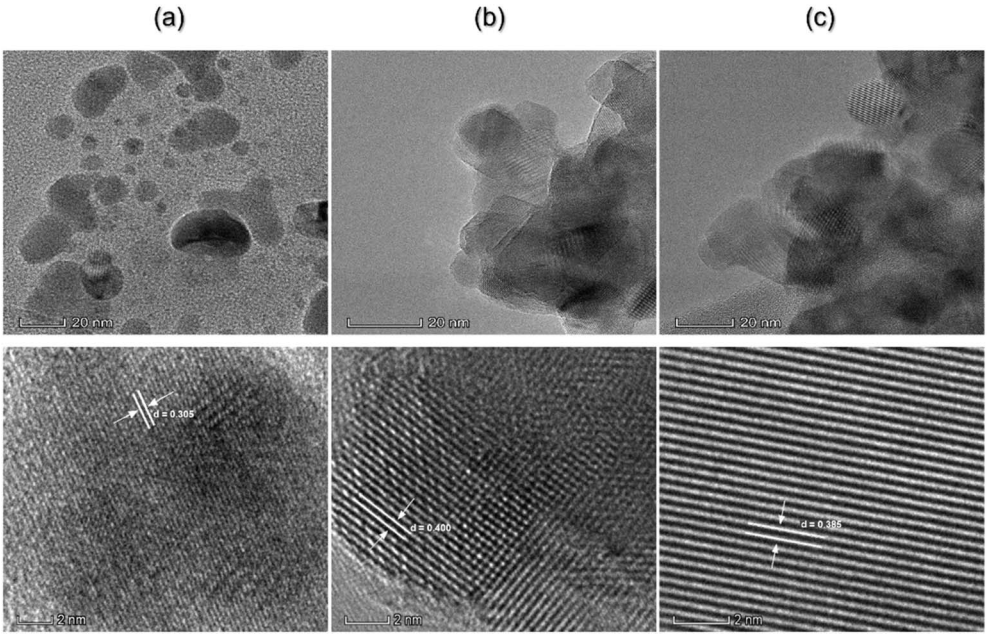

Fig. 8 TEM and HRTEM images of (a) KNPs, (b) Fe_3O_4@KNPs, and (c) the Fe_3O_4@KNPs-Cu(II) nanocomposite.

homogeneous dispersion of iron and copper across the nanocomposite surface. The even distribution of these elements highlights the successful incorporation of Fe_3O_4 and the efficient adsorption of Cu(II), ensuring a consistent elemental composition throughout the material. Additionally, ICP-OES analysis reveals a copper content of 8.3 g kg^{-1} in Fe_3O_4@KNPs-Cu(II), further validating the effective loading of Cu(II) onto the nanocomposite.

The AFM images depict the progressive morphological modifications of KNPs at different functionalization stages, aligning with the SEM observations. The pristine KNPs (Fig. 7a) display a relatively smooth surface with minimal irregularities. After the addition of Fe_3O_4 nanoparticles (Fig. 7b), the surface roughness increases significantly, exhibiting sharp, irregular structures, confirming the successful integration of magnetic nanoparticles onto the keratin matrix. Following the adsorption of Cu(II) ions (Fig. 7c), the surface remains rough but becomes more uniform, with rounded features replacing the sharp edges observed in the previous stage. This transformation, consistent with SEM analysis, suggests that the adsorbed Cu(II) ions not only enhance the uniformity of the surface morphology but also influence the overall topographical structure, further supporting the efficient interaction between copper ions and the Fe_3O_4@KNPs nanocomposite.

The shape and size of the nanoparticles were examined using transmission electron microscopy (TEM) and high-resolution transmission electron microscopy (HRTEM). The TEM images revealed that the KNPs had a spherical shape, with sizes ranging from 4 to 10 nm. Some larger kidney-shaped nanoparticles, exceeding 20 nm, were also observed, possibly due to agglomeration (Fig. 8a). These findings were consistent with the results obtained from SEM. In Fig. 8b, TEM and HRTEM images of the Fe_3O_4@KNPs are depicted. The TEM images showed nanoparticles with particle sizes ranging from 10 to 20 nm, exhibiting a relatively spherical but imperfect shape. The nanocomposite exhibits a core-shell-like structure, characterized by an uneven grayscale contrast, suggesting the presence of a central Fe_3O_4 core surrounded by a shell-like arrangement. This outer layer, composed of KNPs, appears as branched extensions distributed around the core, with an estimated thickness of approximately 3 nm.[60] At very high magnifications, a Fe_3O_4 crystal lattice was observed, aligned along the [3 1 1] direction with a *d*-spacing of 0.257 nm, indicating the high quality of the synthesized material.[76] Similarly, Fig. 8c shows particles with sizes ranging from 10 to 20 nm, aligned along the [2 0 0] direction with a *d*-spacing of 0.297 nm.

The thermal stability of KNPs and Fe_3O_4@KNPs, and the impact of copper solution concentration on thermal stability were investigated using thermogravimetric analysis (TGA) (Fig. 9a) and differential thermogravimetry (DTG) (Fig. 9c). The TG curve of KNPs displayed two discernible phases of weight loss, with the initial mass loss (10%) attributed to the evaporation of physisorbed water.[69] Subsequently, the weight loss observed in the temperature range of 100 to 300 °C was primarily associated with the keratin skeletal degradation and approximately 70% of the original weight was lost in this region.[77] The magnetic Fe_3O_4@KNPs particles show a similar thermal decomposition profile to that of KNPs, *i.e.*, there are two different weight losses in the TGA thermogram. However, the weight loss of Fe_3O_4@KNPs is very different from that of KNPs. The conformational changes of keratin and the additional bridging between Fe_3O_4 and keratin enhanced the thermal stability of keratin in Fe_3O_4@KNPs, and only 26% of the original weight was lost; the final decomposition temperature of Fe_3O_4@KNPs was higher than that for pure keratin. A lower degradation temperature caused by the incorporation of

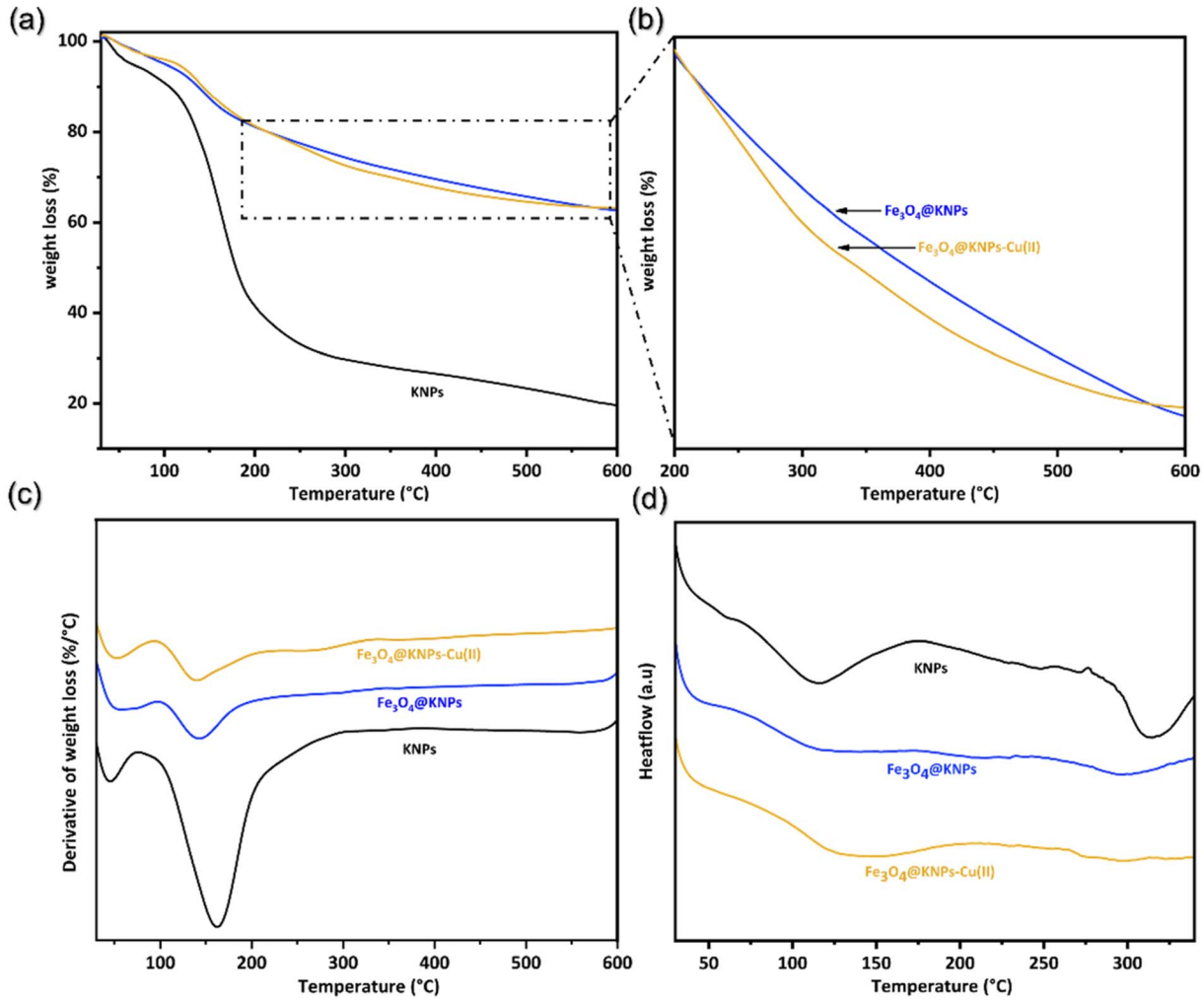

Fig. 9 (a) TGA thermograms of the KNPs, Fe_3O_4@KNPs and Fe_3O_4@KNPs-Cu(II), (b) TGA thermograms of Fe_3O_4@KNPs and Fe_3O_4@KNPs-Cu(II), and (c) DTG (d) and DSC curves.

Cu(II) metal ions into the Fe_3O_4@KNPs structure can be observed (Fig. 9b), which leads to a slight reduction in thermal stability. Overall, TGA results indicate that our Fe_3O_4@KNPs-Cu(II) nanocomposite could be used as a catalytic material in the temperature ranges chosen for our reactions.

The thermal properties of the synthesized materials were investigated using Differential Scanning Calorimetry (DSC), as shown in Fig. 9d. In the DSC thermogram of the KNPs, an initial endothermic peak was observed at 116.0 °C, corresponding to the dehydration process within the keratin matrix. Subsequently, a broader peak at 315.7 °C was observed, indicating the crystalline melting of the protein and the deformation of the α-helix network.[77] The DSC profiles of Fe_3O_4-coated KNPs showed a shift in the initial endothermic peak temperature to a higher value of 127.5 °C compared to KNPs (116.0 °C). For Fe_3O_4@-KNPs-Cu(II) samples, broad temperature ranges along with a shift to higher temperatures were observed, suggesting a broad distribution of crystallite perfection. Interestingly, the Fe_3O_4-coated KNPs showed an absence of crystalline melting temperatures, unlike the KNPs. This deviation may be attributed to the protection of α-helix structures within the KNPs, leading to a transition towards a more amorphous form.

Preparation of 2-substituted benzimidazo[1,2-*a*]pyrimidin-4(10*H*)-one 3a–c

We began our study with the preparation of benzimidazo[1,2-*a*] pyrimidin-4-one compounds **3a–c** through the cyclo-condensation reaction of 2-aminobenzimidazole **1** with different β-ketoesters **2a–c** including phenyl, an electron-donating group (Me) and an electron-withdrawing group (CF_3).

To optimize the reaction conditions, we screened a range of solvents, including xylene, toluene, *N*,*N*-dimethylformamide (DMF) and ethanol (EtOH). The reaction was also conducted under solvent-free conditions using silica as a solid support, both under conventional heating and microwave irradiation (Table 2).

The obtained results indicate that xylene and toluene (entries 1 and 2, Table 2), as apolar solvents, yielded moderate amounts of the cyclocondensed product **3a** achieving 68% yield

Table 2 Optimization of the cyclocondensation reaction of 2-aminobenzimidazole **1** with ethyl benzoylacetate **2a**

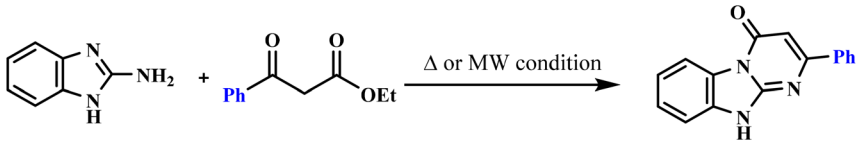

1 **2a** **3a**

		Heating conditions		Microwave conditions		Yield (%)[b]	
Entry[a]	Solvent	T (°C)	t (h)	T (°C)	t (h)	Δ	MW
1	Xylene	140	0.5	100	0.5	68	Traces
2	Toluene	110	1.0	100	1.0	65	Traces
3[c]	Xylene	—	—	140	0.25	—	92
4[d]	EtOH	78	24	100	3.0	76	48
5	DMF	153	0.5	153	0.5	78	81
6[c]	DMF	—	—	153	0.09	—	38
7[e]	Neat	100	0.5	100	0.17	Traces	95

[a] 2-Aminobenzimidazole **1** (1 mmol) and ethyl benzoylacetate **2a** (1.1 mmol) under heating by reflux and in a closed Teflon vessel under microwave (MW) conditions. [b] Isolated yield under heating conditions (and isolated yield under MW conditions). [c] The reaction was operated in an open vessel. [d] The reaction was not completed under closed vessel MW irradiation. [e] The reaction was operated in an open vessel, using silica gel supported reagents under heating and microwave solvent-free conditions. The microwave temperature was measured by using an infrared thermometer.

after 30 minutes and 65% yield after 60 minutes, respectively, under conventional reflux conditions. However, only traces of product **3a** were identified in a closed reaction vessel under microwave irradiation (entries 1 and 2, Table 2), at the same temperature and for the same time defined under conventional heating. It should be noted that the temperature could not reach the reflux temperature of the solvents and stabilized at 100 °C, even if microwave irradiation time is extended to 2 h. This is likely due to the use of apolar solvents (toluene and xylene), which are transparent to microwaves, and so microwave energy is absorbed by the substrates. However, the use of xylene in an open vessel was convenient, despite its weak microwave absorption, and the reaction was remarkably accelerated to give the final product **3a** with excellent yield (92%) after 15 min of microwave irradiation with total evaporation of the solvent. Consequently, the microwave heating observed can be attributed to the polarity of the substrates and/or the polar transition state.[78] It is important to note that temperature and pressure control during the microwave reaction is extremely important to adjust the microwave power and maintain the temperature and pressure at the desired levels.

On the other hand, conventional heating in EtOH (entry 4, Table 2), a polar protic solvent, at reflux for 24 hours provided a relatively high yield of 76% of **3a**, probably because of its hydrogen-bonding capability and ability to stabilize polar intermediates, which enhances reaction efficiency. However, microwave heating in EtOH in a closed vessel for 3 hours (entry 4, Table 2) led to an uncompleted reaction with a yield of 48%. This can be explained by the difficult release of polar molecules (H_2O and EtOH) through the two reversible cyclocondensation reaction steps under MW irradiation with high pressure in a closed vessel.[79] Moreover, a high concentration of ethanol could also lead to over-solvation of the reactants and a decrease in the reaction rate. However, in a closed vessel under MW, ethanol appeared better than xylene and toluene, yielding 48% against traces of product **3a** (entries 1, 2 and 4, Table 2).

However, successful synthesis of compound **3a** through conventional heating treatment was achieved in 0.5 hour by using DMF as a polar aprotic solvent (entry 5, Table 2). Therefore, a yield of 78% was obtained by conventional heating, which was in agreement with the values reported in the literature.[80] Using a specific microwave digestion system equipped with a closed pressure vessel in a well-defined electric field. We showed an improvement in the yield of product **3a** with increasing average absorbed power at a constant total absorbed energy, yielding 81% of **3a** (entry 5, Table 2). Performing the reaction in DMF in an open vessel under MW irradiation provided the desired product **3a** in a low yield (38%) after 5 min at temperatures above 153 °C. The reaction gave complicated mixtures of decomposed products and impurities (entry 6, Table 2).

In spite of the good results obtained in xylene under open vessel MW irradiation (entry 3, Table 2), we focused on a clean and eco-friendly synthesis strategy. For this purpose, the reaction between 2-aminobenzimidazole **1** and β-ketoester **2a** was investigated in an open vessel under MW and solvent-free conditions, by using silica as a solid support, a catalyst and a dehydrating agent, which can generally accelerate the cyclocondensation reaction (entry 7, Table 2).[81] Under these conditions, the cyclocondensation was found to have the highest yield (95%) after just 10 min of microwave irradiation at 100 °C. The use of microwave irradiation was proved necessary, as the

same reaction conducted at 100 °C, leaving the other reaction parameters unchanged, produced only traces of product **3a** (entry 7, Table 2). This shows the importance of impregnation on silica, which has a synergistic effect on reaction catalysis. To evaluate the applicability of the method, we next used two other β-ketoester derivatives, bearing electron-donating (CH_3) and electron-withdrawing (CF_3) substituents in the ketone carbonyl group, to give high yields of the desired cyclocondensed products **3b** (97%) and **3c** (98%). In all cases, the reaction was clean and no by-products were identified. This approach not only displayed the benefits of mesoporous SiO_2 and microwave-assisted reactions but also underscored their importance within a sustainable chemistry context. These products were characterized by using ^{1}H NMR, ^{13}C NMR, ^{19}F NMR, FT-IR, and ESI-MS analysis and the melting point.

Sequential one-pot two-step synthesis of 1,4-disubstituted 1,2,3-triazole-pyrimido-benzimidazoles 5a–x using a novel Fe_3O_4@KNPs-Cu(II) magnetic catalyst

In order to optimize a protocol for synthesizing 1,4-disubstituted 1,2,3-triazole-pyrimido-benzimidazoles *via* a sequential one-pot two-step approach, a model reaction was investigated. This reaction involved a cyclocondensed compound **3a**, propargyl bromide and azidoglucose with various copper(II) sources in aqueous ethanol. The impact of different reaction parameters including the base and activation sources (classical heating or ultrasound cavitation) was also systematically examined. The results obtained are summarized in Table 3.

To evaluate the efficiency of the one-pot, two-step approach, many optimisation reaction conditions were established (entries 1–7, Table 3). First, the reactive intermediate *N*-propargyl pyrimido-benzimidazole **4a**, was generated *in situ via* a propargylation reaction between the cyclocondensed compound **3a** and propargyl bromide in the presence of K_2CO_3 either by heating at 80 °C or under sonication at 55 °C. The subsequent CuAAC click reaction with azidoglucose was most effective when catalyzed by the Fe_3O_4@keratin-Cu(II) nanocomposite (10 wt%) under ultrasonic cavitation using a needle probe with about 15 mm depth of immersion in ethanol/water (2 : 1) (*v*/*v*). Under these conditions, the final product **5a** was obtained in an excellent yield of 86% within just 2 h, compared to 69% over 48 h under magnetic stirring (entry 5, Table 3). This optimization demonstrates the synergistic effect of both ultrasound activation and copper immobilization on the nanocatalyst surface, which prevents chelation by the dipolarophile and significantly accelerates the reaction. However, under classical catalytic conditions, $CuSO_4$ (20 mol%)/(NaAsc) (60 mol%), the reaction did not occur and only traces of product **5a** were formed even after 3 days of magnetic stirring (entries 1 and 2, Table 3).

These differences in catalytic performance may be attributed to the nature of the Cu(II) species in the reaction. In the case of $CuSO_4$/NaAsc, copper ions remain free in the reaction medium and the intermediate **4a** can chelate Cu(II), reducing its efficiency as Cu(II) becomes less available for the click reaction. This phenomenon was observed in several molecules containing nitrogen or oxygen atoms, where copper(I,II) was found to be chelated through coordination interactions.[41b,c] In contrast, the Cu(II) ions in the nanocomposite are strongly bound to the keratin surface, preventing any undesirable undesirable chelation. Therefore, this copper ion immobilization appears to be an effective method for the second step of the one-pot sequential reaction. Also, it is evident that ultrasound cavitation greatly enhances the reaction particularly by reducing the reaction time from 72 hours to just 2 hours by increasing the

Table 3 Optimization of sequential one-pot two-step synthesis of 1,4-disubstituted 1,2,3-triazole-pyrimido-benzimidazoles **5a**

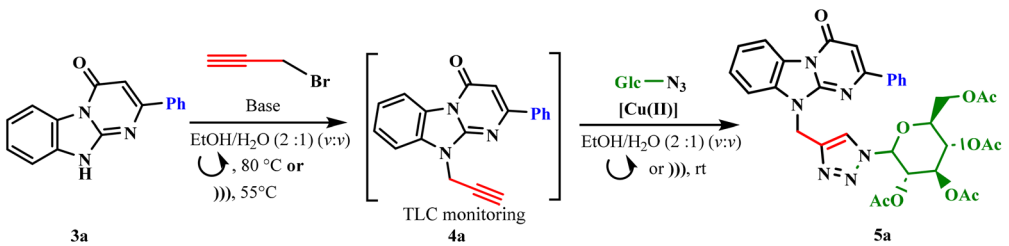

3a 4a 5a

Entry[a]	Base	Catalyst (load)	Classical heating		Ultrasound cavitation[b]	
			Time (h)	Yield (%)[c]	Time (h)	Yield (%)[c]
1[d]	DIPEA	$CuSO_4$/NaAsc (0.2/0.6)	72	Traces	3	11
2[d]	K_2CO_3	$CuSO_4$/NaAsc (0.2/0.6)	72	Traces	3	13
3[d]	K_2CO_3	$CuSO_4$/NaAsc (0.5/1)	72	24	3	38
4	K_2CO_3	Fe_3O_4@KNPs/Cu(II) (5 wt%)	72	46[d]	3	65
5	**K_2CO_3**	**Fe_3O_4@KNPs/Cu(II) (10 wt%)**	**48**	**69**	**2**	**86**
6	K_2CO_3	Fe_3O_4@KNPs/Cu(II) (15 wt%)	48	71	2	87
7	K_2CO_3	Fe_3O_4@KNPs (10 wt%)	48	nr	2	nr

[a] The reaction was performed using **3a** (1 mmol), propargyl bromide (1.1 mmol), and azidoglucose (1.2 mmol) base (2 mmol) in EtOH/H_2O (2/1, *v*/*v*) (15 mL) with a Cu(II) catalyst under heating and ultrasound cavitation. [b] The second step reaction was thermostated at room temperature. [c] Isolated yield of **5a**. [d] The reaction was not completed.

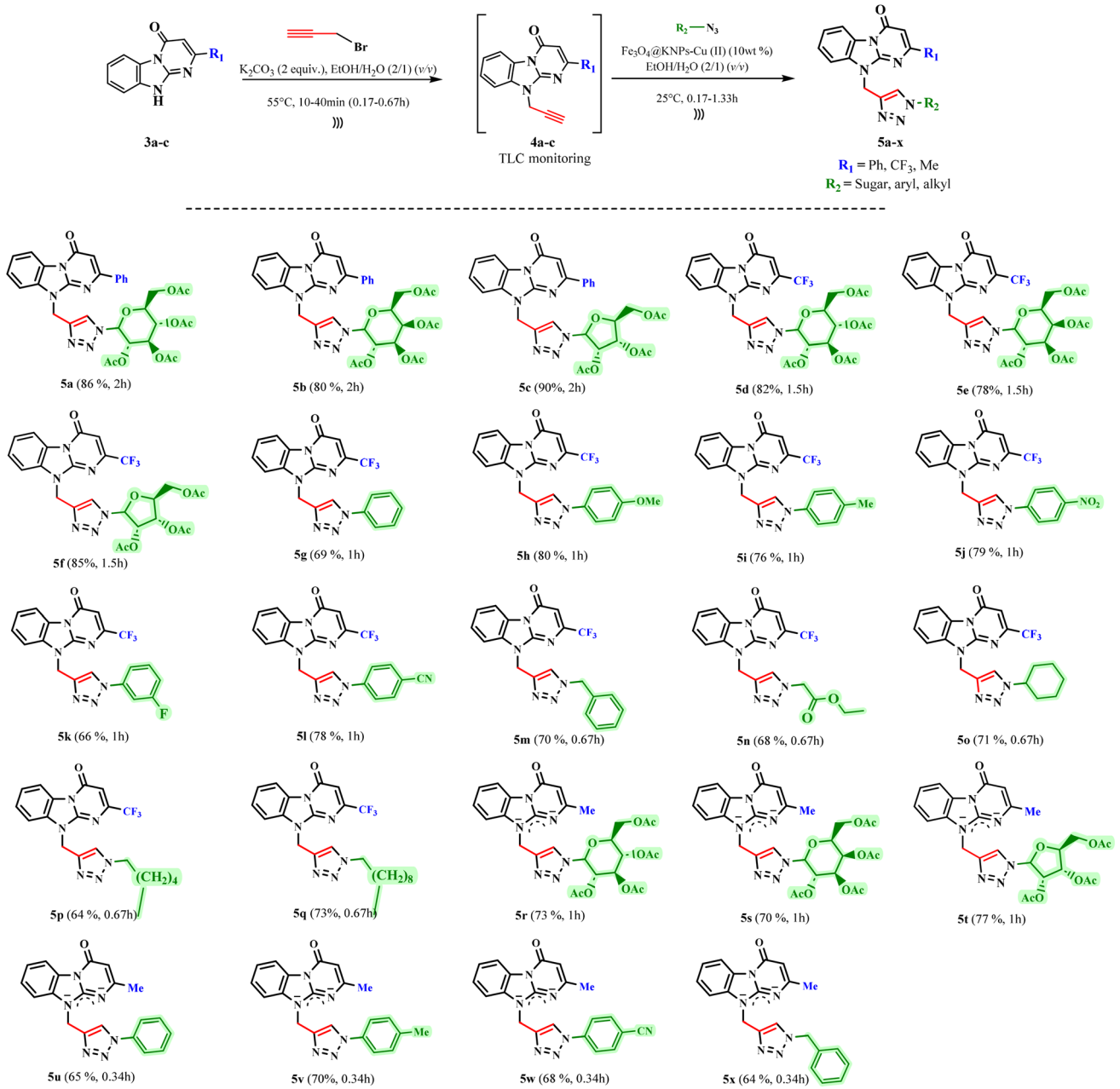

Scheme 2 Synthesis of 1,4-disubstituted 1,2,3-triazole-pyrimido-benzimidazole derivatives **5a–x**.

catalytic amount to 10 wt%, representing a 36-fold acceleration. This remarkable improvement can be attributed to the effects of ultrasound-induced cavitation which substantially accelerates the reaction and boosts yields. The cavitation phenomenon involves the collapse of microbubbles within the heterogeneous solid–liquid system triggered by the intense acoustic pressure of the ultrasound waves.[82] This process promotes efficient mass transfer between the phases, enhancing reagent contact and facilitating their interaction ultimately leading to increased reactivity and improved reaction outcomes.[83] Additionally, when Fe_3O_4@KNPs was used at 10 wt%, the second reaction step did not occur (nr) under both ultrasound and heating conditions (entry 7, Table 3). However, only the formation of intermediate **4a** was observed. This result confirms the essential role of copper(II) in catalyzing the click reaction.

After optimizing the experimental conditions, we explored the scope of this new sequential one-pot two-step approach for the synthesis of novel 1,4-disubstituted 1,2,3-triazole-pyrimido-benzimidazole derivatives **5a–x** using sonotrode activation (Scheme 2). The process started with the propargylation reaction and proceeded to the 1,3-dipolar cycloaddition with Fe_3O_4@KNPs-Cu(II) (10 wt%) in an ethanol–water (EtOH : H_2O) (2 : 1) solvent system. This strategy proved to be highly efficient and fully compatible with our optimized conditions, and generated a series of new 1,4-disubstituted 1,2,3-triazole-pyrimido-benzimidazole derivatives in good to excellent yields (64–

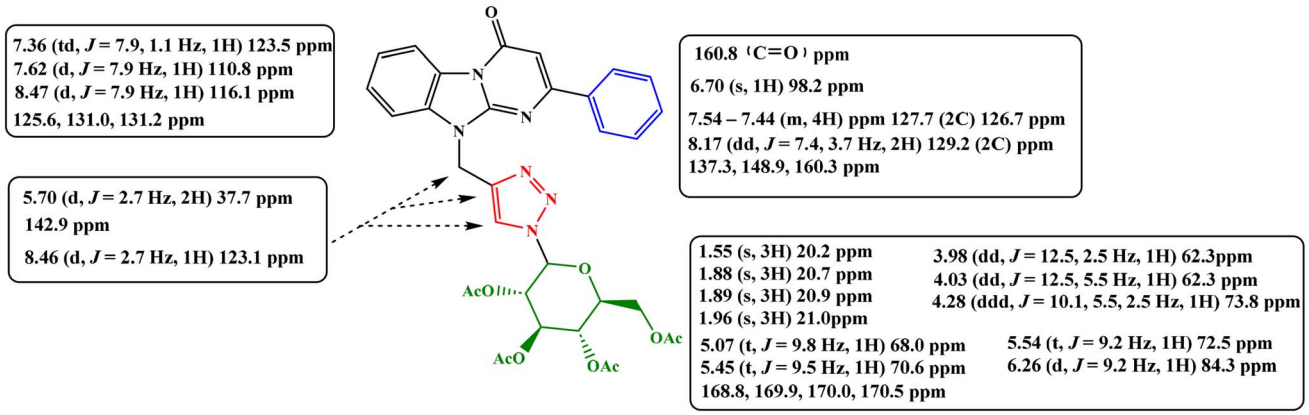

Fig. 10 ^{1}H and ^{13}C NMR characterization of compound **5a**

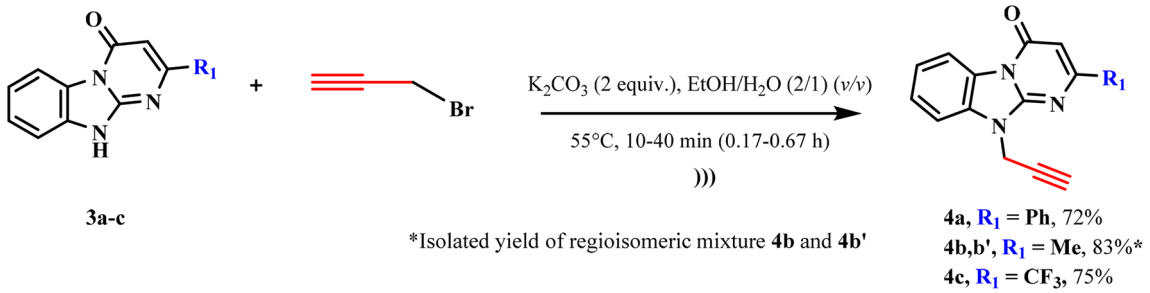

Scheme 3 Synthesis route of dipolarophiles *N*-propargyl pyrimido-benzimidazole **4a–c**.

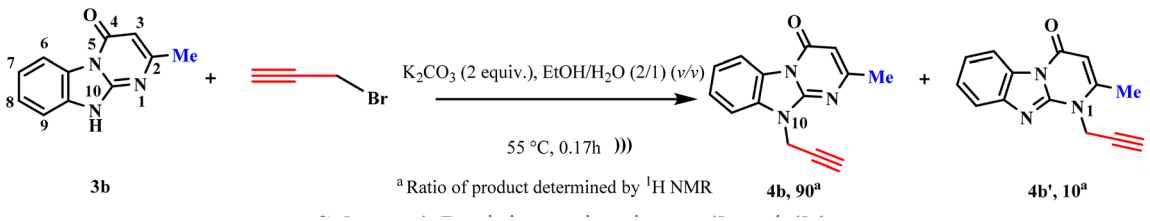

Scheme 4 Regioisomeric mixture of **4b** and **4b′**.

90%). This was achieved by using various substituted cyclocondensed compounds (R_1 = Ph, Me or CF_3) **3a–c** and by changing the substituted sugar azides, to either pentose (ribose) or hexoses (glucose and galactose) and aryl or alkyl azides.

A comprehensive structural analysis of all synthesized products was performed using FT-IR, ^{1}H NMR, ^{13}C NMR,^{19} F NMR and HRMS (see the ESI†). It should be noted that compounds **5r–x** ($R_1 = CH_3$) were obtained as a mixture of two regioisomeric cycloadducts starting from dipolarophile **4b**.

As an example, the ^{1}H NMR spectrum of the final product **5a** (Fig. 10) exhibited a doublet at δ 8.46 ppm (J = 2.7 Hz) corresponding to the CH-triazolic proton. A singlet at δ 6.70 ppm indicated the presence of the H-pyrimidic proton, while another doublet at δ 5.70 ppm (J = 2.7 Hz) was assigned to the CH_2-methylene group. The structure of the glucose fragment was identified by four singlets at δ 1.55, 1.88, 1.89, and 1.96 ppm attributed to the CH_3 groups of the (OAc) functionalities, and two double doublets (dd) at δ 3.98 and 4.03 ppm, corresponding to the CH_2-methylene group. The aromatic protons appeared in the range of δ 7.36 to 8.47 ppm. The ^{13}C NMR spectrum displayed two signals at δ 142.9 and 123.1 ppm assigned to the *C*-triazolic carbons. The amidic (C=O) carbon appeared at δ 160.8 ppm and a signal at δ 37.7 ppm was attributed to the *C*-methylene group. Additionally, four signals at δ 20.2, 20.7, 20.9, and 21.0 ppm corresponded to the *C*-methyl groups of the (OAc) functionalities, while another set of signals at δ 168.8, 169.9, 170.0, and 170.5 ppm indicated the C=O carbons of the (OAc) groups. The aromatic carbons were identified at δ 160.3, 148.9, 137.3, 131.2, 131.0, 129.2 (2C), 127.7 (2C), 126.7, 125.6, 123.5, 116.1, and 110.8 ppm.

Last, we investigated the proposed structures of intermediates **4a–c** as novel dipolarophiles, which had not previously been reported in the literature. To this end, we carried out a propargylation reaction with various cyclocondensed

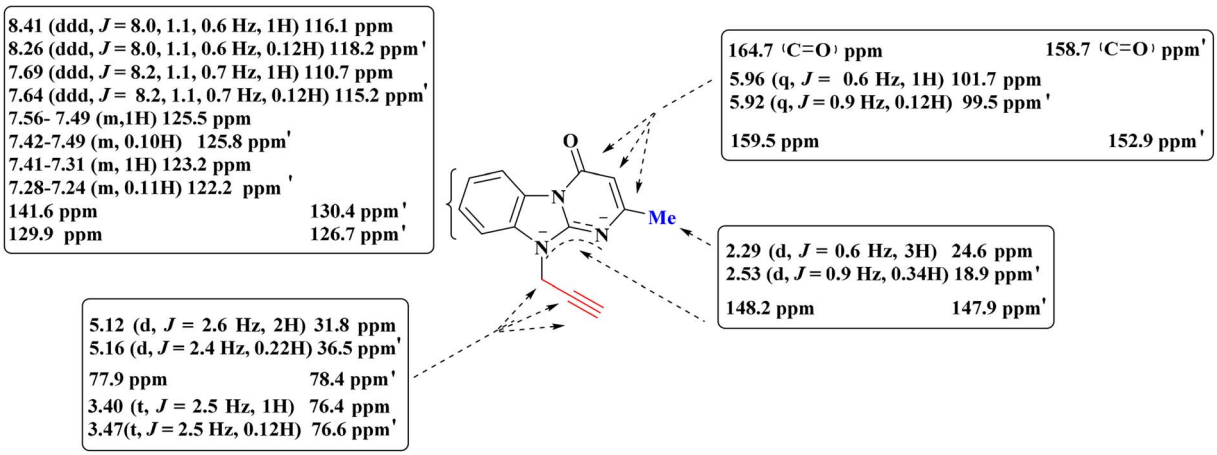

Fig. 11 ^{1}H and ^{13}C NMR characterization of regioisomeric mixture **4b** and **4b′**.

compounds **3a–c** in the presence of propargyl bromide with potassium carbonate (K_2CO_3) as the base in a solvent system EtOH : H_2O (2 : 1) at 55 °C for 0.17–0.67 h under ultrasonic cavitation (Scheme 3).

This alkylation reaction revealed a notable regioselectivity at the imidazole N-10 atom. For compounds **3a** and **3c**, which respectively contain phenyl (Ph) and trifluoromethyl (CF_3) groups at position C-2 of the pyrimidine ring, the reaction proceeded with high regioselectivity yielding **4a** and **4c** as single regioisomers obtained with good yields of 72% and 75% after 0.67 h and 0.43 h, respectively. In contrast, when the methyl group (Me) was present at the same position (compound **3b**), the alkylation resulted in the formation of a mixture of two isomeric products **4b** and **4b′** as shown in Scheme 4. There is limited literature addressing the regioselectivity of alkylation in cases where a methyl group is specifically located in this

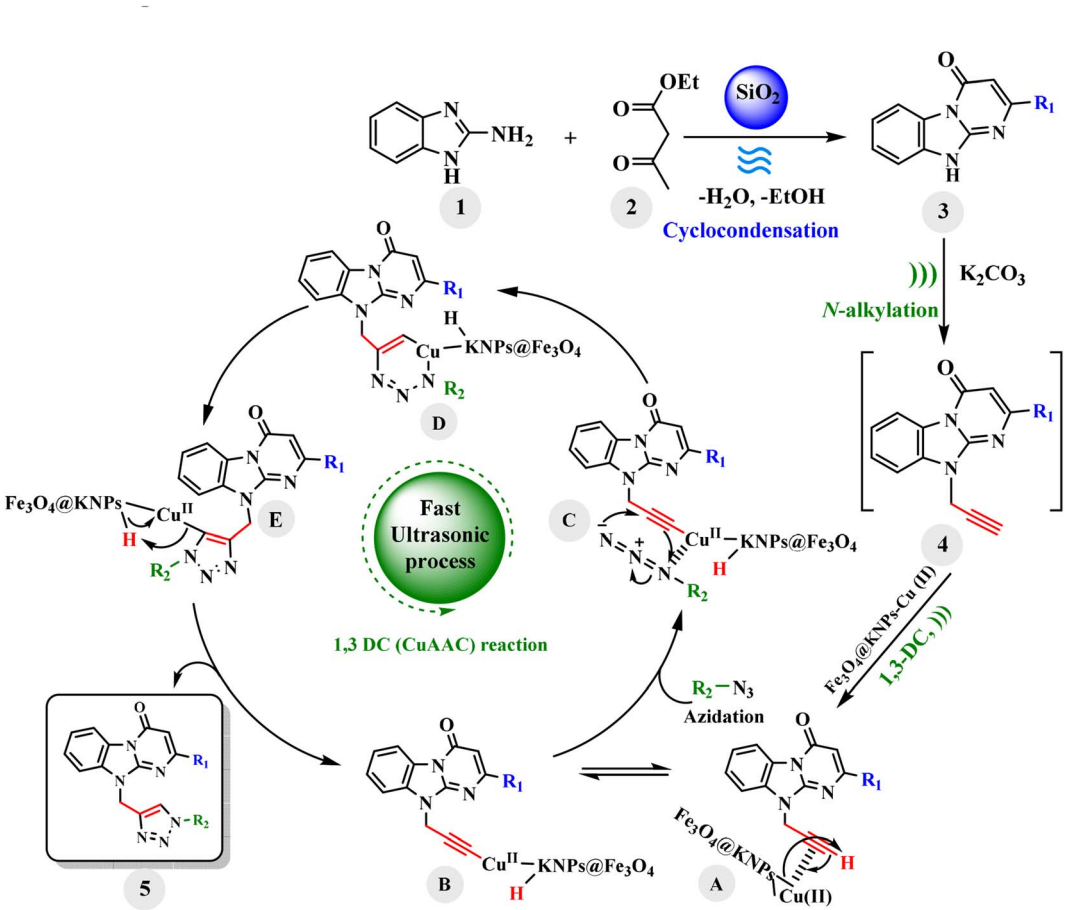

Fig. 12 Plausible mechanism for the Fe_3O_4@KNPs-Cu(II) catalyzed 1,3-dipolar cycloaddition (CuAAC) reaction.

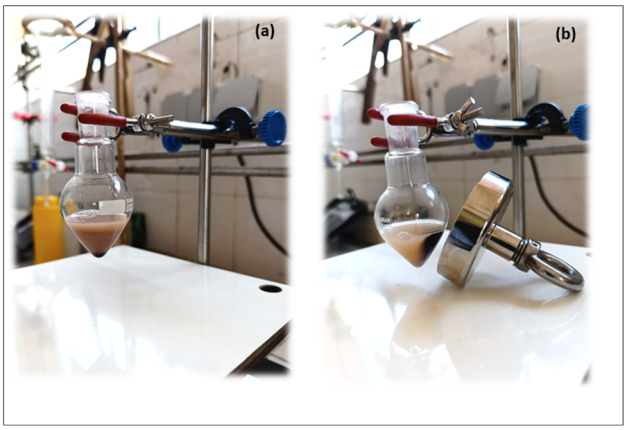

Fig. 13 (a) One-pot two-step synthesis of product **5a** using the Fe_3O_4@KNPs-Cu(II) catalyst under ultrasound irradiation. (b) Separation of the catalyst from the medium using an external magnet.

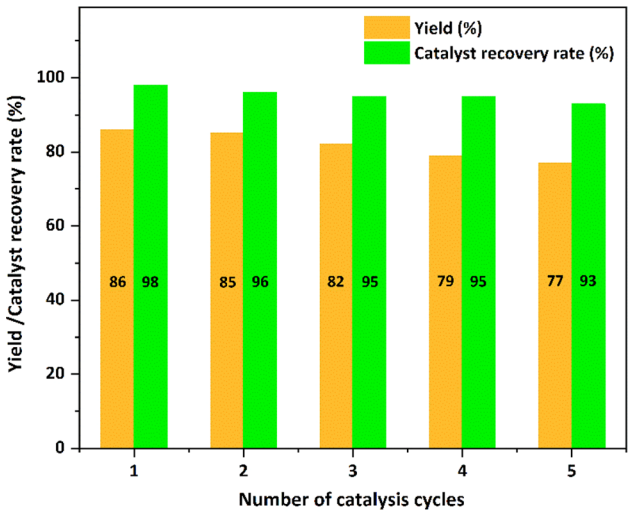

Fig. 14 Recyclability of the Fe_3O_4@KNPs-Cu(II) catalyst for one-pot two-step synthesis of product **5a**.

position.[80,84] These studies consistently show that alkylation predominantly occurs at the N-10 atom as observed in our results with a regioisomer ratio of 9 : 1 (**4b** : **4b′**) determined by ^{1}H NMR. This alkylation of the pyrimidine ring was preferentially promoted by the adjacent methyl group at position 2 in contrast to the phenyl and trifluoromethyl groups, which can be attributed to steric hindrance effects. The relatively small methyl group exerts minimal steric hindrance relative to the propargyl group allowing for a possible approach of the alkylating agent to the N-1 atom whereas the larger phenyl and trifluoromethyl groups induce significant steric repulsion restricting the accessibility to the N-1 site and leading to a more regioselective alkylation. The electronic effects are not a major factor in the observed phenomenon.

The ^{1}H NMR spectra of regioisomers **4b** and **4b′** reveal distinct signals for each isomer as depicted in Fig. 11. For the minor isomer, a downfield doublet at δ 2.53 ppm corresponding to the ($-CH_3$) group appears with a coupling constant $J = 0.9$ Hz, in contrast to δ 2.29 ppm and $J = 0.6$ Hz observed in the major isomer. The CH_2-propargylic protons for the minor isomer resonate as a doublet at δ 5.16 ppm with $J = 2.4$ Hz, while the major isomer shows a similar signal at δ 5.12 ppm with $J =$ 2.16 Hz. A triplet at δ 3.47 ppm is assigned to the ($-C\equiv CH$) terminal propargylic proton in the minor isomer with $J = 2.5$ Hz, whereas the major isomer presents this peak at δ 3.40 ppm maintaining the same coupling constant. Additionally, the H-pyrimidic proton appears as a quadruplet at δ 5.92 ppm with J = 0.9 Hz for the minor isomer and at δ 5.96 ppm with $J = 0.6$ Hz for the major isomer. Aromatic protons are located between δ 7.31 to 8.41 ppm for the more prevalent isomer compared to δ 7.24 to 8.26 ppm for the minor one. The ^{13}C NMR spectra further differentiate the regioisomers, with three notable propargyl group signals at δ 77.9, 76.4, and 31.8 ppm for the major isomer and δ 78.4, 76.6, and 36.5 ppm for the minor one. Additionally, the amidic (C=O) carbon appears at δ 164.7 ppm for the major component and at δ 158.7 ppm for the minor component and the aromatic carbons were detected at the following chemical shifts: from δ 101.7 to 148.2 ppm for the major product and δ 99.5 to 147.9 ppm for the minor product.

The position of the *N*-propargyl group in the studied heterocyclic system was determined through a two-dimensional NMR experiment (^{1}H–^{1}H NOESY). Several recrystallizations were performed on compound **4b**, allowing us to isolate a small fraction of the major compound. The NOESY experiment clearly showed an ^{1}H–^{1}H uncorrelation between the ($-CH_3$) group and the ($-C\equiv CH$) terminal propargylic proton which confirms the N-10 alkylation of the major product (see the ESI†).

A comprehensive mechanism for the synthesis of 1,4-disubstituted 1,2,3-triazole-pyrimido-benzimidazole derivatives 5

The mechanism proceeds through three distinct steps (Fig. 12). The first step involves a cyclocondensation reaction, leading to the formation of compound **3** under MW. It is suggested that

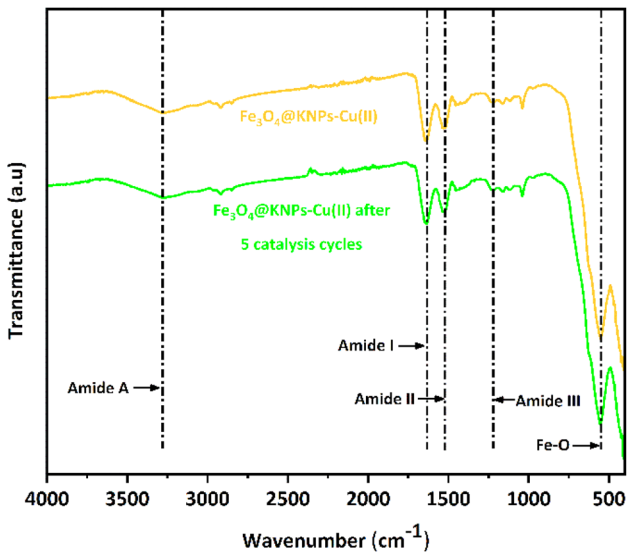

Fig. 15 FT-IR spectra of the as-prepared Fe_3O_4@KNPs-Cu(II) and after five cycles of catalytic tests.

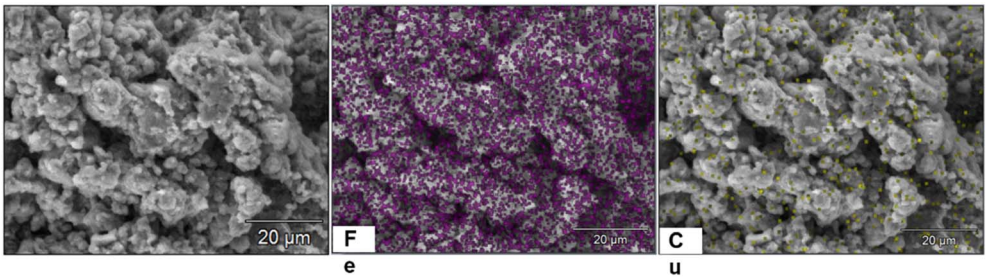

Fig. 16 SEM, Fe, and Cu elemental mapping image of Fe_3O_4@KNPs-Cu(II) after five cycles of catalytic tests.

the reaction proceeds through a polar amidic transition state which is effectively stabilized under the influence of a microwave electric field. This stabilization therefore induces a lowering of the activation energy (ΔG), thereby facilitating the cyclization process. This highlights the specific non-thermal microwave effects in the reaction, which accelerates the transformation and improves overall reaction efficiency.[85] Next, in a sequential one-pot approach, the cyclocondensed product undergoes a propargylation reaction initiated by its deprotonation through the action of potassium carbonate (K_2CO_3) as a base, to yield an alkyne intermediate **4**. Subsequently, the [3 + 2] azide–alkyne cycloaddition, as the last step, begins with the *in situ* coordination of the terminal alkyne to Fe_3O_4@KNPs-Cu(II) forming a new π-complex **A**. Following this, deprotonation of the terminal alkyne occurs assisted by hydroxyl groups that may be present in the keratin support, leading to the formation of a copper–acetylide complex **B**. Simultaneously, the azide derivatives are activated through coordination with the copper complex **B**. In this process, the linear structure of azide interacts with the activated alkyne, where the electrophilic terminal nitrogen of the azide engages with the alkyne **C**, resulting in the formation of a six-membered copper-containing metallocycle **D**. This step marks the [3 + 2] cycloaddition phase, where the azide nitrogen atoms and the alkyne carbons reorganize to form the triazolide ring along with the formation of the Cu–C bond forming a new complex **E**. Finally, protonation of the triazole–copper complex through a protolysis process leads to the formation of 1,4-disubstituted 1,2,3-triazole-pyrimidobenzimidazole derivatives, while the Fe_3O_4@KNPs-Cu(II) catalyst is regenerated completing the catalytic cycle.

Recyclability of the newly prepared magnetic Fe_3O_4 @KNPs-Cu(II) catalyst

Catalyst recovery remains one of the most critical challenges in both research settings and large-scale production processes.[86] In this study, we examined the reusability of our newly developed Cu(II)-based catalyst. For this purpose, a model reaction was carried out employing the Fe_3O_4@KNPs-Cu(II) nanocomposite catalyst in a one-pot two-step strategy to synthesize the target product **5a** (Table 3, entry 5). Due to its magnetic properties, the catalyst can be effortlessly separated from the reaction mixture using an external magnet (Fig. 13). After thorough washing with appropriate solvents, such as water, methanol and dichloromethane, the catalyst can be dried and reused in subsequent reactions.

As illustrated in Fig. 14, the catalyst maintains its efficiency over at least five cycles, without significant reduction in reaction yield. This indicates that the catalyst not only retains its activity over multiple cycles but also aligns well with the principles of green chemistry, offering a promising approach for cost-effective and environmentally friendly organic transformations. Moreover, we have quantitatively evaluated the catalyst recovery efficiency after each cycle, revealing consistently high values ranging from 98% in the first cycle to 93% after the fifth. This minimal decline over multiple reuses highlights the excellent magnetic recoverability of the nanocatalyst and underscores its structural robustness and operational durability under the applied reaction conditions, by using weak basic aqueous media and sonications.

The structural stability of the nanocomposite catalyst was assessed after five successive cycles using FT-IR spectroscopy, revealing no significant alterations in its composition. As shown in Fig. 15, the IR spectra of Fe_3O_4@KNPs-Cu(II) before and after the recycling process exhibit consistent vibrational bands corresponding to both the keratin framework and the magnetic matrix. The retention of these characteristic bands confirms that the nanocomposite preserves its structural integrity, demonstrating resilience and stability even after multiple reuse cycles.

The morphology and elemental composition of the recovered catalyst were examined using SEM and EDX analysis, as shown in Fig. 16. The SEM images reveal that the surface structure of the recycled catalyst remains largely unchanged compared to that of the fresh material. Additionally, elemental mapping confirms the uniform distribution of iron and copper on the KNP surface even after five cycles. This finding is further supported by ICP-OES analysis, which indicates a copper content of 6.7 g kg^{-1} in Fe_3O_4@KNPs-Cu(II) after repeated use. The minimal copper leaching observed underscores the catalyst's high stability and durability across multiple cycles.

Conclusions

A novel and environmentally friendly nanocatalyst made of inexpensive copper metal(II) immobilized on Fe_3O_4@KNPs has been successfully prepared and characterized using various techniques, including FT-IR, XRD, SEM-EDX, ICP-OES, AFM,

TEM, HRTEM, TGA, and DSC analyses. This new magnetic heterogeneous nanocomposite proved to be an effective catalyst for the click reaction, considered a very difficult step when using free Cu(II) ions under conventional Sharpless conditions. This highly active, selective and green catalyst provides products **5a–x** in good to excellent yields (64–90%) in compounds **5a–x** within short reaction times (20–120 min) and under very mild reaction conditions using ethanol–water (EtOH : H_2O) (2 : 1) as a green solvent system under ultrasonic cavitation. This efficient new approach involves the propargylation of benzimidazo[1,2-*a*] pyrimidin-4(10*H*)-one **3a–c**, leading to the *in situ* formation of three terminal alkynes **4a–c** which then undergo the 1,3-dipolar cycloaddition (CuAAC) reaction with various sugar, aryl, and alkyl azides. The cyclocondensed compounds **3a–c** were previously prepared through an eco-friendly cyclocondensation reaction between 2-aminobenzimidazole **1** and β-ketoesters **2a–c** in an open vessel under solvent-free conditions, employing silica as a solid support under microwave irradiation. A comprehensive structural analysis of all synthesized products was performed using FT-IR, ^{1}H NMR, ^{13}C NMR,^{19} F NMR and HRMS. This protocol is efficient, cost-effective, and environmentally friendly, requiring only a low catalyst loading (10 wt%) in the click reaction, with a remarkable 36-fold acceleration compared to the classical method.[37] Furthermore, the nanocomposite [Fe_3O_4@KNPs-Cu(II)] was easily recovered using an external magnet and reused for over five consecutive cycles without significant loss of its catalytic performance. Finally, the immobilization of copper(II) ions appears to be a good alternative strategy to avoid undesirable chelation by alkynes **4a–c** often encountered in an aqueous medium.[87] This work underscores the potential of keratin-based materials as promising biosupports for designing eco-friendly nanocatalysts in heterocyclic chemistry. Future investigations will focus on expanding the scope of this nanocatalyst toward other *N*-heterocycles, particularly those with strong coordinating functionalities, and exploring its performance in large scale and continuous-flow systems to further enhance its industrial applicability.

Experimental section

Materials and methods

All organic solvents were acquired from commercial sources and used without further purification. All the reagents were purchased from commercial sources (Merck, Sigma-Aldrich, Thermo Scientific and Riedel-de Haein) and used without further purification. Column chromatography was carried out employing silica gel 60 (230–400, 13 mesh, 0.040–0.063 mm) and during elution, a cyclohexane and ethyl acetate mixture was used. Analytical thin layer-chromatography (TLC) has been performed on pre-coated silica gel plates (Kieselgel 60 F254, E. Merck, Germany), and all compounds were visualized by UV irradiation (longwave at 365 nm or shortwave at 254 nm). All compounds were characterized by using ^{1}H, ^{13}C and ^{19}F NMR analysis, FTIR, HRMS and the melting point. NMR (nuclear magnetic resonance) spectra were recorded on a JNM-ECZ500R/S1 FT NMR system (JEOL) (500 MHz; 11.74 T). Proton, carbon and fluorine magnetic resonance spectra (^{1}H NMR, ^{13}C NMR and ^{19}F NMR) were recorded using tetramethylsilane (TMS) in DMSO-d_6 (^{1}H NMR at 2.50 ppm; ^{13}C NMR at 40.0 ppm). Splitting patterns are denoted as follows: s (singlet), d (doublet), t (triplet), m (multiplet), dd (double doublet), and td (triple doublet). The chemical shifts are reported in δ ppm relative to TMS (0 ppm) and coupling constants J are reported in hertz (Hz). Electrospray ionization – mass spectra (ESI-MS) were recorded on an Agilent Technologies 1260 Infinity II LC/MSD, and the samples were diluted in methanol. The Fourier transform-infrared (FTIR) experiments were conducted using a JASCO FT-IR-4600 spectrophotometer. For each sample, scans were obtained at up to 10 different positions within the spectral range of 4000–400 cm^{-1}. High resolution mass spectra (HRMS) were measured using electrospray ionization (ESI) and the measurements were performed in the positive ion mode with a resolution of 140 000 for m/z 200. Melting points were determined on a Köfler bench system. The structural and compositional characteristics of KNPs, Fe_3O_4@KNPs, and Fe_3O_4@KNPs-Cu(II) were thoroughly analyzed using various techniques. FT-IR spectroscopy (FTIR-4600, Jasco) was employed to identify the functional groups within the range of 4000–400 cm^{-1}. Crystalline structures of the materials were examined through X-ray diffraction (XRD) using a Bruker AXS D4 diffractometer with Cu Kα radiation ($\lambda = 1.54$ Å), recording data over the 2θ range of 10° to 80°. Surface morphology was investigated using a Thermo Fisher Scientific Quattro scanning electron microscope (SEM) operating at an accelerating voltage of 15 kV. The elemental composition and spatial distribution of elements were determined through energy-dispersive X-ray (EDX) analysis. Atomic force microscopy (AFM) was utilized to explore the surface topography of the prepared materials. For AFM analysis, 10 mg of each sample was dispersed in 1 mL of water, and a thin film was prepared by depositing 20 μL of the solution onto a glass coverslip and allowing it to dry for 30 minutes before scanning with a Nanosurf Easyscan 2 AFM. The morphological features and particle size of the synthesized materials were further visualized through transmission electron microscopy (TEM) using an FEI Tecnai G2 F20 S/TEM at an accelerating voltage of 200 kV. TEM grids were prepared by placing a drop of the particle suspension onto a carbon-coated copper grid and drying under a lamp. Copper content in the composite was quantified by inductively coupled plasma optical emission spectroscopy (ICP-OES) with an Avio 200 instrument (PerkinElmer). Finally, the thermal stability of the materials was assessed through thermogravimetric analysis (TGA) using a Thermo Cahn HS/Versa Therm and differential scanning calorimetry (DSC) with a SENSYS EVO 131 system.

Keratin extraction and preparation of KNPs

Chicken feathers (CF), obtained from a local poultry processing facility (Casablanca, Morocco), were pre-treated with a 20% ethanol solution to remove fats and impurities. After drying, 50 g of CF were dissolved in 1 L of 1 M H_2O_2 neutralized with 1% NaOH under mechanical agitation at 60 °C for 1.5 hours. The resulting solution was centrifuged at 9000 rpm for 10 minutes

to remove insoluble residues. The supernatant was subsequently introduced into 200 mL of 1 M HCl under ultrasonic treatment, leading to the breakdown of microparticles into nanoscale particles. KNPs were collected by centrifugation at 9000 rpm for 30 minutes and washed with distilled water.

Preparation of keratin-modified Fe_3O_4 nanoparticles (Fe_3O_4@KNPs)

Keratin-modified Fe_3O_4 nanoparticles were synthesized *via* the co-precipitation method. Specifically, 1.6 g of $FeCl_2 \cdot 4H_2O$ and 3.7 g of $FeCl_3 \cdot 6H_2O$ were dissolved in an aqueous dispersion of KNPs (2 g/100 mL). Ammonium hydroxide was added dropwise under continuous stirring at room temperature, facilitating the co-precipitation of Fe^{2+} and Fe^{3+} ions. Stirring continued for 30 minutes, after which the Fe_3O_4@KNPs were magnetically separated, washed with deionized water and dried overnight in a desiccator.

Preparation of the Fe_3O_4@KNPs-Cu(II) nanocatalyst

To synthesize the Fe_3O_4@KNPs-Cu(II) catalyst, 1 g of Fe_3O_4@KNPs was added to 25 mL of an aqueous copper sulfate solution (0.1 M $CuSO_4 \cdot 5H_2O$) and stirred overnight at room temperature. The catalyst was then magnetically separated, washed with water and dried overnight in a desiccator.

General procedure for synthesis of 2-substituted benzimidazo[1,2-*a*]pyrimidin-4(10*H*)-one 3a–c

Silica gel (SiO_2, 1.0 g, 230–400 mesh, pH 6–7) was added to a mixture of 2-aminobenzimidazole **1** (1 mmol, 133 mg) and β-ketoesters **2a–c** (1.1 mmol) in dichloromethane (20 mL). The reaction mixture was stirred for 5 minutes, and then concentrated to dryness under reduced pressure. The resulting solid was irradiated by microwaves with a power of 1200 W in a Teflon open vessel for 10 minutes. The maximum temperature measured with a non-contact infrared thermometer was around 100 °C. Upon completion of the reaction (monitored by TLC), the mixture was allowed to cool to room temperature and dichloromethane (DCM, 2 × 15 mL) was added. The solid catalyst was separated by filtration and washed with additional DCM (10 mL). The combined DCM extracts were concentrated under reduced pressure. The resulting crude product was then purified by recrystallization in ethanol (EtOH), yielding the desired compounds **3a–c** with high purity.

General procedure for sequential one-pot two-step synthesis of 1,4-disubstituted 1,2,3-triazole-pyrimido-benzimidazole derivatives 5a–x

In a pear-shaped flask, 2-substituted benzimidazo[1,2-*a*]pyrimidin-4(10*H*)-one **3a–c** (1 mmol, 200 mg), propargyl bromide (1.1 mmol) and potassium carbonate (K_2CO_3) (2 mmol) were dissolved in a 2 : 1 (*v*/*v*) mixture of EtOH/H_2O (15 mL). The reaction mixture was sonicated using a sonotrode for 10–40 min, resulting in a gradual temperature increase from 25 °C to 55 °C. The temperature was maintained at 55 °C and monitored with a noncontact infrared thermometer. Upon completion of the reaction (monitored by TLC), the azide (1.2 mmol) and Fe_3O_4@KNPs-Cu(II) catalyst (10 wt%) were added. The mixture was sonicated with the sonotrode for 0.17–1.33 h at 25 °C, maintained constant using a double-walled glass reactor. After completion of the reaction (monitored by TLC), the catalyst was separated with an external magnet and washed with DCM (3 × 10 mL) to extract the adsorbed organic material. The solvent was evaporated under reduced pressure and the crude product was purified by column chromatography on silica gel using a cyclohexane : ethylacetate (3 : 2) eluent, yielding the desired products **5a–x**.

Spectral data of 2-substituted benzimidazo[1,2-*a*]pyrimidin-4(10*H*)-one 3a–c

2-Phenylbenzo[4,5]imidazo[1,2-*a*]pyrimidin-4(10*H*)-one (3a). White solid, yield 95% (lit.[80] 75%), Mp 247–249 °C, TLC (cyclohexane/AcOEt, 6/4, *v*/*v*) $R_f = 0.57$. FTIR (ATR, cm^{-1}): 3034, 2966, 1666, 1545, 1524, 1465, 1450, 1240, 739, 695. ^{1}H NMR (500 MHz, DMSO-d_6): $\delta = 8.42$ (d, $J = 8.0$ Hz, 1H), 8.07 (dd, $J = 8.0$, 3.0 Hz, 2H), 7.49 (d, $J = 8.0$ Hz, 1H), 7.45 (m, 4H), 7.29 (td, $J = 7.7$, 1.3 Hz, 1H), 6.57 (s, 1H). ^{13}C NMR (126 MHz, DMSO-d_6): $\delta = 161.2$, 160.4, 150.2, 137.6, 131.5, 130.8, 129.2 (2C), 127.5 (2C), 126.7, 126.3, 122.3, 116.2, 111.7, 97.4. MS (ESI$^+$): $m/z = 262.0$ [M + H]$^+$, 532.2 [2 M + H]$^+$, 545.1 [2 M + Na]$^+$, 561.1 [2 M + K]$^+$. The NH proton of the benzimidazole ring was not observed in the ^{1}H NMR spectrum, likely due to rapid prototropic exchange and solvation effects in DMSO-d_6 as previously reported for similar systems.[88]

2-Methylbenzo[4,5]imidazo[1,2-*a*]pyrimidin-4(10*H*)-one (3b). White solid, yield 97% (lit.[80] 60%), Mp 274–276 °C, TLC (cyclohexane/AcOEt, 6/4, *v*/*v*) $R_f = 0.14$. FTIR (ATR, cm^{-1}): 3079, 2683, 1681, 1643, 1609, 1567, 1452, 1362, 758, 744. ^{1}H NMR (500 MHz, DMSO-d_6): $\delta = 8.32$ (d, $J = 7.8$ Hz, 1H), 7.48 (d, $J = 7.8$ Hz, 1H), 7.38 (td, $J = 7.8$, 1.2 Hz, 1H), 7.23 (td, $J = 7.8$, 1.2 Hz, 1H), 5.78 (s, 1H), 2.26 (s, 3H). ^{13}C NMR (126 MHz, DMSO-d_6): $\delta = 159.9$ (2C), 149.0, 127.4, 126.0, 121.8, 115.7 (2C), 114.2, 98.9, 22.30. MS (ESI$^+$): $m/z = 200.1$ [M + H]$^+$, 399.1 [2 M + H]$^+$, 421.1 [2 M + Na]$^+$. The NH proton of the benzimidazole ring was not observed in the ^{1}H NMR spectrum, likely due to rapid prototropic exchange and solvation effects in DMSO-d_6 as previously reported for similar systems.[88]

2-(Trifluoromethyl)benzo[4,5]imidazo[1,2-*a*]pyrimidin-4(10*H*)-one (3c). Brown solid, yield 98% (lit.[80] 55%), Mp 268–270 °C, TLC (cyclohexane/AcOEt, 6/4, *v*/*v*) $R_f = 0.69$. FTIR (ATR, cm^{-1}): 3446, 2987, 1686, 1590, 1534, 1491, 1473, 1276, 1138, 735, 722. ^{1}H NMR (500 MHz, DMSO-d_6): $\delta = 8.41$ (d, $J = 7.8$ Hz, 1H), 7.64 (s, 1H), 7.52 (d, $J = 7.8$ Hz, 1H), 7.45 (td, $J = 7.8$, 1.3 Hz, 1H), 7.28 (td, $J = 7.8$, 1.1 Hz, 1H), 6.30 (s, 1H). ^{13}C NMR (126 MHz, DMSO-d_6): $\delta = 159.7$, 151.4 (q, $J_{C-F} = 33.9$ Hz), 150.9, 131.9, 127.2, 126.2, 122.7, 116.4, 112.3, 121.9 (q, $J_{C-F} = 275$ Hz), 98.8 (q, $J_{C-F} = 3.07$ Hz). ^{19}F NMR (471 MHz, DMSO-d_6): $\delta = -68.47$ (s, 3F). MS (ESI$^+$): $m/z = 254.0$ [M + H]$^+$, 507.1 [2 M + H]$^+$.

Spectral data of alkyne intermediates 4a–c

2-Phenyl-10-(prop-2-yn-1-yl)benzo[4,5]imidazo[1,2-*a*]pyrimidin-4(10*H*)-one (4a). White solid, yield 72%, Mp 245–247 °C, TLC (cyclohexane/AcOEt, 6/4, *v*/*v*) $R_f = 0.48$. FTIR (ATR, cm^{-1}): 3284, 3073, 2960, 2925, 1668, 1589, 1573, 1537, 1473, 1375, 746,

758, 697, 683. ^{1}H NMR (500 MHz, DMSO-d_6): δ = 8.47 (d, J = 8.0 Hz, 1H), 8.19 (dd, J = 6.9, 2.8 Hz, 2H), 7.74 (d, J = 8.0 Hz, 1H), 7.56 (td, J = 7.5, 1.2 Hz, 1H), 7.49 (m, 3H), 7.40 (td, J = 7.5, 1.2 Hz, 1H), 6.71 (s, 1H), 5.28 (d, J = 2.4 Hz, 2H), 3.45 (t, J = 2.4 Hz, 1H). ^{13}C NMR (126 MHz, DMSO-d_6): δ = 160.6, 160.2, 148.4, 137.1, 131.1, 130.8, 129.3 (2C), 127.7 (2C), 126.9, 125.6, 123.4, 116.2, 110.8, 98.4, 77.9, 76.4, 32.0. HRMS: calcd. for $C_{19}H_{13}N_3O^+$ ([M + Na]$^+$): 322.09563, found: 322.09286.

2-Methyl-10-(prop-2-yn-1-yl)benzo[4,5]imidazo[1,2-*a*]pyrimidin-4(10*H*)-one (4b). White solid, Mp 228–230 °C, TLC (cyclohexane/AcOEt, 6/4, *v*/*v*) R_f = 0.24. FTIR (ATR, cm^{-1}): 3184, 3072, 2922, 2114, 1681, 1609, 1582, 1538, 1473, 1166, 763, 716, 700. ^{1}H NMR (500 MHz, DMSO-d_6): δ = 8.41 (d, J = 7.8 Hz, 1H), 7.69 (d, J = 7.8 Hz, 1H), 7.52 (td, J = 7.7, 1.1 Hz, 1H), 7.36 (td, J = 7.8, 1.1 Hz, 1H), 5.97 (s, 1H), 5.12 (d, J = 2.4 Hz, 2H), 3.40 (t, J = 2.4 Hz, 1H), 2.29 (s, 3H).· ^{13}C NMR (126 MHz, DMSO-d_6): δ = 164.7, 159.5, 148.2, 130.4, 126.7, 125.5, 123.2, 116.1, 110.7, 101.7, 77.9, 76.4, 31.8, 24.6. HRMS: calcd. for $C_{14}H_{11}N_3O^+$ ([M + H]$^+$): 238.09804, found: 238.09586.

Mixture of regioisomers (4b/4b′)(9/1). Brown solid, yield 83%, Mp 225–227 °C, TLC (cyclohexane/AcOEt, 6/4, *v*/*v*) R_f = 0.3/0.5. FTIR (ATR, cm^{-1}): 3233, 3186, 2921, 2114, 1677, 1608, 1584, 1539, 1473, 1413, 1166, 764, 739, 722, 699. ^{1}H NMR (500 MHz, DMSO-d_6): δ = 8.41 (ddd, J = 8.0, 1.1, 0.6 Hz, 1H), 8.26 (ddd, J = 8.0, 1.1, 0.6 Hz, 0.12H)′, 7.69 (ddd, J = 8.2, 1.1, 0.7 Hz, 1H), 7.64 (ddd, J = 8.2, 1.1, 0.7 Hz, 0.12H)′, 7.56–7.49 (m, 1H), 7.42–7.49 (m, 0.10H)′, 7.41–7.31 (m, 1H), 7.28–7.24 (m, 0.11H)′, 5.96 (q, J = 0.6 Hz, 1H), 5.92 (q, J = 0.9 Hz, 0.12H)′, 5.12 (d, J = 2.6 Hz, 2H), 5.16 (d, J = 2.4 Hz, 0.22H)′, 3.40 (t, J = 2.5 Hz, 1H), 3.47 (t, J = 2.5 Hz, 0.12H)′, 2.29 (d, J = 0.6 Hz, 3H), 2.53 (d, J = 0.9 Hz, 0.34H)′. ^{13}C NMR (126 MHz, DMSO-d_6): δ = 164.7, 158.7′, 159.5, 152.9′, 148.2, 147.9′, 141.6, 130.4′, 129.9, 126.7′, 125.5, 125.8′, 123.2, 122.2′, 116.1, 118.2′, 110.7, 115.2′, 101.7, 99.5′, 77.9, 78.4′, 76.4, 76.6′, 31.8, 36.5′, 24.6, 18.9.

10-(Prop-2-yn-1-yl)-2-(trifluoromethyl)benzo[4,5]imidazo[1,2-*a*]pyrimidin-4(10*H*)-one (4c). Brown solid, yield 75%, Mp 197–199 °C, TLC (cyclohexane/AcOEt, 6/4, *v*/*v*) R_f = 0.76. FTIR (ATR, cm^{-1}): 3105, 2998, 1687, 1590, 1560, 1486, 1472, 1272, 1136, 771, 754, 740, 689. ^{1}H NMR (500 MHz, DMSO-d_6): δ = 8.46 (d, J = 7.5 Hz, 1H), 7.79 (d, J = 7.6 Hz, 1H), 7.61 (td, J = 7.5, 1.2 Hz, 1H), 7.44 (td, J = 7.6, 1.1 Hz, 1H), 6.56 (s, 1H), 5.20 (d, J = 2.6 Hz, 2H), 3.45 (t, J = 2.6 Hz, 1H). ^{13}C NMR (126 MHz, DMSO-d_6): δ = 159.3, 150.8 (q, J_{C-F} = 34.5 Hz), 148.9, 130.7, 127.5, 125.3, 124.0, 121.7 (q, J_{C-F} = 275.1 Hz), 116.5, 111.2, 101.1 (q, J_{C-F} = 3.0 Hz), 77.4, 76.9, 32.4. ^{19}F NMR (471 MHz, DMSO-d_6): δ = −68.60 (s, 3F). HRMS: calcd. for $C_{14}H_8F_3N_3O^+$ ([M + H]$^+$): 292.06977, found: 292.06671.

Spectral data of 1,4-disubstituted 1,2,3-triazole-pyrimido-benzimidazole derivatives 5a–x

(2*S*,3*S*,4*R*,5*S*)-2-(Acetoxymethyl)-6-(4-((4-oxo-2-phenylbenzo[4,5]imidazo[1,2-*a*]pyrimidin-10(4*H*)-yl)methyl)-1*H*-1,2,3-triazol-1-yl)tetrahydro-2*H*-pyran-3,4,5-triyl triacetate (5a). White solid, yield 86%, Mp 241–243 °C, TLC (cyclohexane/AcOEt, 4/6, *v*/*v*) R_f = 0.45. FTIR (ATR, cm^{-1}): 3072, 1752, 1680, 1592, 1576, 1475, 1411, 1270, 1042, 1030, 759, 744, 697. ^{1}H NMR (500 MHz, DMSO-d_6): δ = 8.47 (d, J = 7.9 Hz, 1H), 8.46 (d, J = 2.7 Hz, 1H), 8.17 (dd, J = 7.4, 3.7 Hz, 2H), 7.62 (d, J = 7.9 Hz, 1H), 7.54–7.44 (m, 4H), 7.36 (td, J = 7.9, 1.1 Hz, 1H), 6.70 (s, 1H), 6.26 (d, J = 9.2 Hz, 1H), 5.70 (d, J = 2.7 Hz, 2H), 5.54 (t, J = 9.2 Hz, 1H), 5.45 (t, J = 9.5 Hz, 1H), 5.07 (t, J = 9.8 Hz, 1H), 4.28 (ddd, J = 10.1, 5.5, 2.5 Hz, 1H), 4.03 (dd, J = 12.5, 5.5 Hz, 1H), 3.98 (dd, J = 12.5, 2.5 Hz, 1H), 1.96 (s, 3H), 1.89 (s, 3H), 1.88 (s, 3H), 1.55 (s, 3H). ^{13}C NMR (126 MHz, DMSO-d_6): δ = 170.5, 170.0, 169.9, 168.8, 160.8, 160.3, 148.9, 142.9, 137.3, 131.2, 131.0, 129.2 (2C), 127.7 (2C), 126.7, 125.6, 123.5, 123.1, 116.1, 110.8, 98.2, 84.3, 73.8, 72.5, 70.6, 68.0, 62.3, 37.7, 21.0, 20.9, 20.7, 20.2. HRMS: calcd. for $C_{33}H_{32}N_6O_{10}^+$ ([M + H]$^+$): 673.22582, found: 673.21954.

(2*S*,3*R*,4*R*,5*S*)-2-(Acetoxymethyl)-6-(4-((4-oxo-2-phenylbenzo[4,5]imidazo[1,2-*a*]pyrimidin-10(4*H*)-yl)methyl)-1*H*-1,2,3-triazol-1-yl)tetrahydro-2*H*-pyran-3,4,5-triyl triacetate (5b). White solid, yield 80%, Mp 242–244 °C, TLC (cyclohexane/AcOEt, 4/6, *v*/*v*) R_f = 0.71. FTIR (ATR, cm^{-1}): 3071, 1736, 1669, 1589, 1574, 1475, 1411, 1219, 1041, 1021, 763, 741, 693. ^{1}H NMR (500 MHz, DMSO-d_6): δ = 8.47 (d, J = 7.7 Hz, 1H), 8.45 (s, 1H), 8.18 (dd, J = 6.7, 3.0 Hz, 2H), 7.61 (d, J = 8.2 Hz, 1H), 7.50–7.45 (m, 4H), 7.35 (td, J = 8.2, 1.1 Hz, 1H), 6.70 (s, 1H), 6.18 (d, J = 9.2 Hz, 1H), 5.70 (s, 2H), 5.5 (t, J = 9.3 Hz, 1H), 5.38 (dd, J = 9.3, 3.5 Hz, 1H), 5.35 (dd, J = 3.5, 1.2 Hz, 1H), 4.5 (td, J = 7.4, 3.5 Hz, 1H), 4.05 (dd, J = 11.6, 5.0 Hz, 1H), 3.93 (dd, J = 11.6, 7.4 Hz, 1H), 2.09 (s, 3H), 1.89 (s, 3H), 1.88 (s, 3H), 1.61 (s, 3H). ^{13}C NMR (126 MHz, DMSO-d_6): δ = 170.5, 170.4, 170.0, 168.9, 160.8, 160.3, 148.9, 142.8, 137.2, 131.3, 131.0, 129.2 (2C), 127.7 (2C), 126.7, 125.6, 124.0, 123.1, 116.1, 110.7, 98.2, 84.8, 73.5, 70.8, 68.2, 67.8, 62.0, 37.7, 21.0, 20.9, 20.8, 20.3. HRMS: calcd. for $C_{33}H_{32}N_6O_{10}^+$ ([M + H]$^+$): 673.22582, found: 673.22345.

(2*S*,3*S*,4*S*)-2-(Acetoxymethyl)-5-(4-((4-oxo-2-phenylbenzo[4,5]imidazo[1,2-*a*]pyrimidin-10(4*H*)-yl)methyl)-1*H*-1,2,3-triazol-1-yl)tetrahydrofuran-3,4-diyl diacetate (5c). White solid, yield 90%, Mp 173–175 °C, TLC (cyclohexane/AcOEt, 4/6, *v*/*v*) R_f = 0.57. FTIR (ATR, cm^{-1}): 3086, 1734, 1665, 1594, 1588, 1472, 1452, 1271, 1142, 1049, 1021, 742. ^{1}H NMR (500 MHz, DMSO-d_6): δ = 8.46 (d, J = 8.0 Hz, 1H), 8.40 (s, 1H), 8.17 (dd, J = 6.7, 3.0 Hz, 2H), 7.73 (d, J = 8.0 Hz, 1H), 7.50 (td, J = 7.8, 1.1 Hz, 1H), 7.48–7.45 (m, 3H), 7.36 (td, J = 7.8, 1.1 Hz, 1H), 6.69 (s, 1H), 6.30 (d, J = 3.3 Hz, 1H), 5.71 (dd, J = 3.3 Hz, 5.4, 3H), 5.50 (dd, J = 6.2, 5.4 Hz, 1H), 4.36 (dd, J = 12.2, 5.4 Hz, 1H), 4.24 (dd, J = 12.2, 3.3 Hz, 1H), 3.99 (dd, J = 12.2, 4.9 Hz, 1H), 2.02 (s, 3H), 2.00 (s, 3H), 1.78 (s, 3H). ^{13}C NMR (126 MHz, DMSO-d_6): δ = 170.4, 170.0, 169.7, 160.8, 160.3, 148.8, 142.7, 137.2, 131.3, 131.0, 129.2 (2C), 127.7 (2C), 126.8, 125.5, 124.6, 123.1, 116.1, 110.8, 98.2, 89.5, 80.3, 73.8, 70.7, 62.9, 37.6, 20.8, 20.7 (2C). HRMS: calcd. for $C_{30}H_{28}N_6O_8^+$ ([M + H]$^+$): 601.20469, found: 601.20367.

(2*S*,3*S*,4*R*,5*S*)-2-(Acetoxymethyl)-6-(4-((4-oxo-2-(trifluoromethyl)benzo[4,5]imidazo[1,2-*a*]pyrimidin-10(4*H*)-yl)methyl)-1*H*-1,2,3-triazol-1-yl)tetrahydro-2*H*-pyran-3,4,5-triyl triacetate (5d). White solid, yield 82%, Mp 239–241 °C, TLC (cyclohexane/AcOEt, 4/6, *v*/*v*) R_f = 0.58. FTIR (ATR, cm^{-1}): 3095, 1734, 1665, 1594, 1588, 1472, 1452, 1271, 1142, 1094, 1021, 742. ^{1}H NMR (500 MHz, DMSO-d_6): δ = 8.47 (d, J = 8.0 Hz, 1H), 8.42 (s, 1H), 7.66 (d, J = 8.2 Hz, 1H), 7.54 (t, J = 7.8 Hz, 1H), 7.42 (t, J = 7.8 Hz, 1H), 6.57 (s, 1H), 6.27 (d, J = 8.9 Hz, 1H), 5.64 (s, 2H), 5.4 (t, J = 9.3 Hz, 1H), 5.47 (t, J = 9.4 Hz, 1H), 5.08 (t, J = 9.6 Hz,

1H), 4.30 (dd, J = 9.8, 5.3 Hz, 1H), 4.05 (dd, J = 12.5, 5.3 Hz, 1H), 3.99 (dd, J = 12.5, 2.4 Hz, 1H), 1.97 (s, 3H), 1.92 (s, 3H), 1.90 (s, 3H), 1.61 (s, 3H). ^{13}C NMR (126 MHz, DMSO-d_6): 170.5, 170.1, 169.9, 168.8, 159.4, 151.0 (q, J_{C-F} = 34.4 Hz), 149.4, 142.4, 131.1, 127.5, 125.4, 123.8, 123.7, 121.46 (q, J_{C-F} = 275.21 Hz), 116.4, 111.2, 100.7 (q, J_{C-F} = 3.2 Hz), 100.8, 84.3, 73.8, 72.5, 70.6, 68.0, 62.2, 38.0, 21.0, 20.9, 20.7, 20.2. ^{19}F NMR (471 MHz, DMSO-d_6): δ = −68.52 (s, 3F). HRMS: calcd. for $C_{28}H_{27}F_3N_6O_{10}^+$ ([M + H]$^+$): 665.18191, found: 665.18054.

(2*S*,3*R*,4*R*,5*S*)-2-(Acetoxymethyl)-6-(4-((4-oxo-2-(trifluoromethyl)benzo[4,5]imidazo[1,2-*a*]pyrimidin-10(4*H*)-yl)methyl)-1*H*-1,2,3-triazol-1-yl)tetrahydro-2*H*-pyran-3,4,5-triyl triacetate (5e). White solid, yield 78%, Mp 183–185 °C, TLC (cyclohexane/AcOEt, 4/6, *v*/*v*) R_f = 0.5. FTIR (ATR, cm^{-1}): 3080, 1734, 1681, 1591, 1589, 1478, 1452, 1272, 1142, 1046, 1022, 751. ^{1}H NMR (500 MHz, DMSO-d_6): δ = 8.46 (d, J = 8.1 Hz, 1H), 8.22 (s, 1H), 7.63 (d, J = 8.2 Hz, 1H), 7.53 (td, J = 8.2, 1.1 Hz, 1H), 7.40 (td, J = 8.1, 1.1 Hz, 1H), 6.48 (s, 1H), 6.08 (d, J = 9.1 Hz, 1H), 5.61 (s, 2H), 5.43 (td, J = 9.1, 3.9 Hz, 1H), 5.35 (d, J = 5.84, 3.9 Hz, 1H), 5.33 (d, J = 6.5, 5.84 Hz, 1H), 4.46 (td, J = 11.6, 6.5 Hz, 1H), 4.06 (dd, J = 11.6, 5.5 Hz, 1H), 3.97 (dd, J = 11.6, 6.8 Hz, 1H), 2.09 (s, 3H), 1.90 (s, 3H), 1.86 (s, 3H), 1.59 (s, 3H). ^{13}C NMR (126 MHz, DMSO-d_6): δ = 170.4, 169.9, 168.9, 159.4, 151.5(q, J_{C-F} = 34.4 Hz), 149.5, 142.1, 131.2, 127.5, 125.4, 123.8 (q, J_{C-F} = 3.4 Hz), 121.8 (q, J_{C-F} = 275.21 Hz), 116.5, 111.1, 100.6, 99.5, 85.2, 81.3, 73.8, 71.0, 68.7, 68.0, 61.8, 38.1, 21.5, 20.7, 20.5, 20.0. ^{19}F NMR (471 MHz, DMSO-d_6): δ = −68.70 (s, 3F). HRMS: calcd. for $C_{28}H_{27}F_3N_6O_{10}^+$ ([M − H]$^-$): 663.16625, found: 663.16583.

(2*S*,3*S*,4*S*)-2-(Acetoxymethyl)-5-(4-((4-oxo-2-(trifluoromethyl)benzo[4,5]imidazo[1,2-*a*]pyrimidin-10(4*H*)-yl)methyl)-1*H*-1,2,3-triazol-1-yl)tetrahydrofuran-3,4-diyl diacetate (5f). Orange viscous oil, yield 85%, TLC (cyclohexane/AcOEt, 4/6, *v*/*v*) R_f = 0.64. FTIR (ATR, cm^{-1}): 3088, 1744, 1691, 1594, 1588, 1477, 1436, 1276, 1141, 1040, 1022, 742. ^{1}H NMR (500 MHz, DMSO-d_6): δ = 8.44 (d, J = 7.6 Hz, 1H), 8.20 (s, 1H), 7.68 (d, J = 8.0 Hz, 1H), 7.53 (td, J = 8.0, 1.3 Hz, 1H), 7.4 (td, J = 7.6, 1.1 Hz, 1H), 6.46 (s, 1H), 6.21 (d, J = 3.4 Hz, 1H), 5.68 (dd, J = 5.5, 3.4 Hz, 1H), 5.61 (s, 2H), 5.42 (t, J = 5.5 Hz, 1H), 4.40–4.32 (m, 1H), 4.20 (dd, J = 12.3, 3.4 Hz, 1H), 4.03 (dd, J = 12.3, 4.7 Hz, 1H), 2.00 (s, 3H), 1.99 (s, 3H), 1.78 (s, 3H). ^{13}C NMR (126 MHz, DMSO-d_6): δ = 170.4, 170.0, 169.7, 159.5, 151.4 (q, J_{C-F} = 34.8 Hz), 149.4, 142.0, 131.2, 127.6, 125.4, 124.2, 124.2, 122.7 (q, J_{C-F} = 275.22 Hz), 116.5, 111.1, 100.6 (q, J_{C-F} = 3.3 Hz), 90.0, 80.7, 74.0, 70.9, 63.0, 38.0, 20.5, 20.4, 20.4. ^{19}F NMR (471 MHz, DMSO-d_6): δ = −68.65 (s, 3F). HRMS: calcd. for $C_{25}H_{23}F_3N_6O_8^+$ ([M + H]$^+$): 593.16078, found: 593.15601.

10-((1-Phenyl-1*H*-1,2,3-triazol-4-yl)methyl)-2-(trifluoromethyl)benzo[4,5]imidazo[1,2-*a*]pyrimidin-4(10*H*)-one (5g). White solid, yield 69%, Mp 265–267 °C, TLC (cyclohexane/AcOEt, 6/4, *v*/*v*) R_f = 0.52. FTIR (ATR, cm^{-1}): 3087, 2989, 2958, 1695, 1592, 1563, 1490, 1475, 1274, 1131, 807, 798, 765, 747. ^{1}H NMR (500 MHz, DMSO-d_6): δ = 8.61 (s, 1H), 8.50 (d, J = 7.9 Hz, 1H), 7.75 (d, J = 8.5 Hz, 1H), 7.73 (dd, J = 7.9, 2.5 Hz, 2H), 7.56 (td, J = 7.9, 1.1 Hz, 1H), 7.51(td, J = 7.9, 1.1 Hz, 2H), 7.45–7.42 (m, 2H), 6.49 (s, 1H), 5.70 (s, 2H). ^{13}C NMR (126 MHz, DMSO-d_6): δ = 159.4, 151.51(q, J_{C-F} = 34.8 Hz), 149.6, 142.6, 137.1, 131.4 (2C), 130.3, 129.4, 127.6, 125.5, 123.9, 122.8, 120.8 (2C), 119.6 (q, J_{C-F} = 274.4 Hz), 116.4, 111.2, 100.7 (q, J_{C-F} = 3.2 Hz), 38.3. ^{19}F NMR (471 MHz, DMSO-d_6): δ = −68.55 (s, 3F). HRMS: calcd. for $C_{20}H_{13}F_3N_6O^+$ ([M + Na]$^+$): 433.10006, found: 433.09692.

10-((1-(4-Methoxyphenyl)-1*H*-1,2,3-triazol-4-yl)methyl)-2-(trifluoromethyl)benzo[4,5]imidazo[1,2-*a*]pyrimidin-4(10*H*)-one (5h). White solid, yield 80%, Mp 223–225 °C, TLC (cyclohexane/AcOEt, 6/4, *v*/*v*) R_f = 0.48. FTIR (ATR, cm^{-1}): 3087, 2945, 2845, 1695, 1592, 1564, 1519, 1441, 1276, 1260, 1133, 835, 823, 765, 743. ^{1}H NMR (500 MHz, DMSO-d_6): δ = 8.64 (s, 1H), 8.48 (d, J = 7.7 Hz, 1H), 7.79 (d, J = 7.7 Hz, 1H), 7.67 (d, J = 9.0 Hz, 2H), 7.56 (td, J = 7.7, 1.1 Hz, 1H), 7.42 (td, J = 7.7, 1.1 Hz, 1H), 7.05 (d, J = 9.0 Hz, 2H), 6.57 (s, 1H), 5.69 (s, 2H), 3.75 (s, 3H). ^{13}C NMR (126 MHz, DMSO-d_6): δ = 159.9, 159.4, 151.1 (q, J_{C-F} = 34.4 Hz), 149.4, 142.3, 131.2, 130.3, 127.5, 125.4, 123.8, 122.6, 122.2 (2C), 122.1 (q, J_{C-F} = 274.4 Hz), 116.4, 115.4 (2C), 111.3, 100.7 (q, J_{C-F} = 3 Hz), 56.0, 38.17. ^{19}F NMR (471 MHz, DMSO-d_6): δ = −68.52 (s, 3F). HRMS: calcd. for $C_{21}H_{15}F_3N_6O_2^+$ ([M + H]$^+$): 441.12868, found: 441.12494.

10-((1-(*p*-Tolyl)-1*H*-1,2,3-triazol-4-yl)methyl)-2-(trifluoromethyl)benzo[4,5]imidazo[1,2-*a*]pyrimidin-4(10*H*)-one (5i). White solid, yield 76%, Mp 261–263 °C, TLC (cyclohexane/AcOEt, 6/4, *v*/*v*) R_f = 0.5. FTIR (ATR, cm^{-1}): 3151, 3088, 1704, 1597, 1568, 1500, 1475, 1284, 1129, 1109, 871, 855, 764, 750. ^{1}H NMR (500 MHz, DMSO-d_6): δ = 8.57 (s, 1H), 8.50 (d, J = 8.2 Hz, 1H), 7.75 (d, J = 8.5 Hz, 1H), 7.61 (d, J = 8.0 Hz, 2H), 7.56 (td, J = 8.2, 1.2 Hz, 1H), 7.43 (td, J = 8.5, 1.1 Hz, 1H), 7.31 (d, J = 8.0 Hz, 2H), 6.49 (s, 1H), 5.69 (s, 2H), 2.32 (s, 3H). ^{13}C NMR (126 MHz, DMSO-d_6): δ = 159.4, 151.5 (q, J_{C-F} = 34.7 Hz), 149.6, 142.5, 139.1, 134.9, 131.4, 130.7 (2C), 127.5, 125.6, 123.8, 122.6, 120.7 (2C), 120.6 (q, J_{C-F} = 274.9 Hz), 116.5, 111.3, 100.6 (q, J_{C-F} = 3.3 Hz), 38.3, 20.9. ^{19}F NMR (471 MHz, DMSO-d_6): δ = −68.54 (s, 3F). HRMS: calcd. for $C_{21}H_{15}F_3N_6O^+$ ([M + H]$^+$): 425.13377, found: 425.12982.

10-((1-(4-Nitrophenyl)-1*H*-1,2,3-triazol-4-yl)methyl)-2-(trifluoromethyl)benzo[4,5]imidazo[1,2-*a*]pyrimidin-4(10*H*)-one (5j). Yellow solid, yield 79%, Mp 253–255 °C, TLC (cyclohexane/AcOEt, 6/4, *v*/*v*) R_f = 0.68. FTIR (ATR, cm^{-1}): 3137, 2931, 1747, 1590, 1556, 1474, 1453, 1276, 1222, 1106, 990, 762, 740. ^{1}H NMR (500 MHz, DMSO-d_6): δ = 8.95 (s, 1H), 8.48 (d, J = 8.0 Hz, 1H), 8.37 (d, J = 9.3 Hz, 2H), 8.08 (d, J = 9.3 Hz, 2H), 7.79 (d, J = 8.2 Hz, 1H), 7.57 (td, J = 8.0, 1.3 Hz, 1H), 7.42 (td, J = 8.2, 1.1 Hz, 1H), 6.58 (s, 1H), 5.74 (s, 2H). ^{13}C NMR (126 MHz, DMSO-d_6): δ = 159.4, 151.1 (q, J_{C-F} = 34.4 Hz), 149.4, 147.3, 143.5, 141.1, 131.2, 127.5, 126.1 (2C), 125.4, 123.9, 123.0, 121.7 (q, J_{C-F} = 280.5 Hz), 121.1 (2C), 116.4, 111.3, 100.8 (q, J_{C-F} = 3.3 Hz), 38.1. ^{19}F NMR (471 MHz, DMSO-d_6): δ = −68.50 (s, 3F). HRMS: calcd. for $C_{20}H_{12}F_3N_7O_3^+$ ([M + H]$^+$): 456.10320, found: 456.09894.

10-((1-(3-Fluorophenyl)-1*H*-1,2,3-triazol-4-yl)methyl)-2-(trifluoromethyl)benzo[4,5]imidazo[1,2-*a*]pyrimidin-4(10*H*)-one (5k). White solid, yield 66%, Mp 241–243 °C, TLC (cyclohexane/AcOEt, 6/4, *v*/*v*) R_f = 0.6. FTIR (ATR, cm^{-1}): 3011, 1685, 1589, 1557, 1456, 1441, 1273, 1136, 901, 821, 768, 749. ^{1}H NMR (500 MHz, DMSO-d_6): δ = 8.80 (s, 1H), 8.49 (d, J = 8.0 Hz, 1H), 7.79 (d, J = 8.2 Hz, 1H), 7.71 (dt, J = 10.0, 2.4 Hz, 1H), 7.67 (dd, J = 8.2, 1.1 Hz, 1H), 7.62–7.53 (m, 2H), 7.44 (td, J = 8.2, 1.1 Hz, 1H), 7.29 (td, J = 8.0, 1.6 Hz, 1H), 6.59 (s, 1H), 5.72 (s, 2H). ^{13}C NMR (126

MHz, DMSO-d_6): δ = 162.9 (d, J_{C-F} = 245.3 Hz), 159.4, 151.0 (q, J_{C-F} = 34.5 Hz), 149.4, 143.1, 138.1 (d, J_{C-F} = 10.4 Hz), 132.4 (d, J_{C-F} = 9.2 Hz), 131.2, 127.6, 125.4, 124.1 (q, J_{C-F} = 274.1 Hz), 123.8, 122.8, 116.4, 116.5 (d, J_{C-F} = 3.1 Hz), 116.1 (d, J_{C-F} = 21.0 Hz), 111.3, 108.1 (d, J_{C-F} = 26.4 Hz), 100.8 (q, J_{C-F} = 3.1 Hz), 38.1. ^{19}F NMR (471 MHz, DMSO-d_6): δ = −68.49 (s, 3F), −110.46 (s, 1F). HRMS: calcd. for $C_{20}H_{12}F_4N_6O^+$ ([M + H]$^+$): 429.10870, found: 429.10495.

4-(4-((4-Oxo-2-(Trifluoromethyl)benzo[4,5]imidazo[1,2-*a*]pyrimidin-10(4*H*)-yl)methyl)-1*H*-1,2,3-triazol-1-yl)benzonitrile (5l). White solid, yield 78%, Mp 249–251 °C, TLC (cyclohexane/AcOEt, 6/4, *v*/*v*) R_f = 0.72. FTIR (ATR, cm^{-1}): 3155, 2921, 2855, 1692, 1594, 1565, 1487, 1473, 1272, 1140, 909, 831, 764, 744. ^{1}H NMR (500 MHz, DMSO-d_6): δ = 8.90 (s, 1H), 8.48 (d, J = 7.9 Hz, 1H), 8.03 (d, J = 9.5 Hz, 2H), 8.01 (d, J = 9.5 Hz, 2H), 7.79 (d, J = 7.9 Hz, 1H), 7.56 (td, J = 7.9, 1.2 Hz, 1H), 7.42 (td, J = 7.9, 1.2 Hz, 1H), 6.58 (s, 1H), 5.73 (s, 2H). ^{13}C NMR (126 MHz, DMSO-d_6): δ = 159.4, 151.1 (q, J_{C-F} = 34.4 Hz), 149.4, 143.4, 139.8, 134.8 (2C), 131.2, 127.5, 125.4, 123.8, 122.8, 121.7 (q, J_{C-F} = 275.0 Hz), 121.0 (2C), 118.6, 116.4, 111.7, 111.3, 100.8 (q, J_{C-F} = 3.0 Hz), 38.1. ^{19}F NMR (471 MHz, DMSO-d_6): δ = −68.50 (s, 3F). HRMS: calcd. for $C_{21}H_{12}F_3N_7O^+$ ([M + Na]$^+$): 458.09531, found: 458.09088.

10-((1-Benzyl-1*H*-1,2,3-triazol-4-yl)methyl)-2-(trifluoromethyl)benzo[4,5]imidazo[1,2-*a*]pyrimidin-4(10*H*)-one (5m). White solid, yield 70%, Mp 215–217 °C, TLC (cyclohexane/AcOEt, 6/4, *v*/*v*) R_f = 0.6. FTIR (ATR, cm^{-1}): 3011, 1685, 1589, 1557, 1472, 1456, 1273, 1136, 768, 749, 724, 692. ^{1}H NMR (500 MHz, DMSO-d_6): δ = 8.45 (d, J = 8.0 Hz, 1H), 8.18 (s, 1H), 7.73 (d, J = 8.0 Hz, 1H), 7.54 (td, J = 8.0, 1.1 Hz, 1H), 7.40 (td, J = 8.0, 1.1 Hz, 1H), 7.33–7.24 (m, 3H), 7.20 (dd, J = 7.9, 1.7 Hz, 2H), 6.54 (s, 1H), 5.60 (s, 2H), 5.52 (s, 2H). ^{13}C NMR (126 MHz, DMSO-d_6): δ = 159.4, 151.0 (q, J_{C-F} = 34.2 Hz), 149.3, 141.8, 136.4, 131.2, 129.2, 128.7, 128.4, 128.4, 128.3, 127.4, 125.3, 124.6, 123.7, 121.7 (q, J_{C-F} = 274.9 Hz), 116.4, 111.3, 100.6 (q, J_{C-F} = 3.3 Hz), 53.4, 38.1.^{19}F NMR (471 MHz, DMSO-d_6): δ = −68.55 (s, 3F). HRMS: calcd. for $C_{21}H_{15}F_3N_6O^+$ ([M + H]$^+$): 425.13377, found: 425.12946.

Ethyl2-(4-((4-oxo-2-(trifluoromethyl)benzo[4,5]imidazo[1,2-*a*]pyrimidin-10(4*H*)-yl)methyl)-1*H*-1,2,3-triazol-1-yl)acetate (5n). White solid, yield 68%, Mp 203–205 °C, TLC (cyclohexane/AcOEt, 6/4, *v*/*v*) R_f = 0.38. FTIR (ATR, cm^{-1}): 2994, 1734, 1687, 1598, 1567, 1476, 1418, 1278, 1225, 1136, 1109, 792, 744. ^{1}H NMR (500 MHz, DMSO-d_6): δ = 8.47 (d, J = 8.1 Hz, 1H), 8.15 (s, 1H), 7.75 (d, J = 8.2 Hz, 1H), 7.56 (td, J = 8.1, 1.2 Hz, 1H), 7.42 (td, J = 8.2, 1.1 Hz, 1H), 6.56 (s, 1H), 5.64 (s, 2H), 5.32 (s, 2H), 4.09 (q, J = 7.1 Hz, 2H),1.13 (t, J = 7.1 Hz, 3H). ^{13}C NMR (126 MHz, DMSO-d_6): δ = 167.6, 159.4, 151.0 (q, J_{C-F} = 34.4 Hz), 149.3, 141.6, 131.2, 127.4, 125.9, 125.3, 123.8, 121.6 (q, J_{C-F} = 275.0 Hz), 116.4, 111.4, 100.7 (q, J_{C-F} = 3.4 Hz), 62.0, 51.0, 38.0, 14.4. ^{19}F NMR (471 MHz, DMSO-d_6): δ = −68.50 (s, 3F). HRMS: calcd. for $C_{18}H_{15}F_3N_6O_3^+$ ([M + H]$^+$): 421.12360, found: 421.11914.

10-((1-Cyclohexyl-1*H*-1,2,3-triazol-4-yl)methyl)-2-(trifluoromethyl)benzo[4,5]imidazo[1,2-*a*]pyrimidin-4(10*H*)-one (5o). Yellow solid, yield 71%, Mp 219–221 °C, TLC (cyclohexane/AcOEt, 6/4, *v*/*v*) R_f = 0.4. FTIR (ATR, cm^{-1}): 2936, 1685, 1588, 1557, 1537, 1474, 1272, 1144, 776, 750. ^{1}H NMR (500 MHz, DMSO-d_6): δ = 8.48 (d, J = 8.2 Hz, 1H), 8.09 (s, 1H), 7.72 (d, J = 8.2 Hz, 1H), 7.55 (td, J = 8.2, 1.2 Hz, 1H), 7.41 (td, J = 8.2, 1.2 Hz, 1H), 6.51 (s, 1H), 5.59 (s, 2H), 4.4 (quint., J = 3.6 Hz, 1H), 1.98 (dd, J = 12.7, 2.9 Hz, 2H), 1.74 (dt, J = 13.7, 3.6 Hz, 2H), 1.70–1.55 (m, 3H), 1.36 (q, J = 12.7 Hz, 2H), 1.17 (q, J = 12.7 Hz, 1H). ^{13}C NMR (126 MHz, DMSO-d_6): δ = 159.3, 151.2 (q, J_{C-F} = 34.3 Hz), 149.4, 141.1, 131.4, 127.4, 125.4, 123.7, 122.4, 121.6 (q, J_{C-F} = 274.7 Hz), 116.4, 111.3, 100.6 (q, J_{C-F} = 3.0 Hz), 59.7, 38.4, 33.2 (2C), 25.2, 25.0 (2C). ^{19}F NMR (471 MHz, DMSO-d_6): δ = −68.52 (s, 3F). HRMS: calcd. for $C_{20}H_{19}F_3N_6O^+$ ([M + H]$^+$): 417.16507, found: 417.16077.

10-((1-Hexyl-1*H*-1,2,3-triazol-4-yl)methyl)-2-(trifluoromethyl)benzo[4,5]imidazo[1,2-*a*]pyrimidin-4(10*H*)-one (5p). White solid, yield 64%, Mp 157–159 °C, TLC (cyclohexane/AcOEt, 6/4, *v*/*v*) R_f = 0.6. FTIR (ATR, cm^{-1}): 3186, 2921, 1677, 1608, 1584, 1539, 1473, 1413, 1166, 764, 739. ^{1}H NMR (500 MHz, DMSO-d_6): δ = 8.46 (d, J = 8.0 Hz, 1H), 8.10 (s, 1H), 7.73 (d, J = 8.2 Hz, 1H), 7.57 (td, J = 8.2, 1.1 Hz, 1H), 7.42 (td, J = 8.0, 1.1 Hz, 1H), 6.55 (s, 1H), 5.60 (s, 2H), 4.25 (t, J = 7.1 Hz, 2H), 1.68 (quint., J = 7.1 Hz, 2H), 1.25–1.03 (m, 6H), 0.74 (t, J = 7.1 Hz, 3H). ^{13}C NMR (126 MHz, DMSO-d_6): δ = 159.4, 151.1 (q, J_{C-F} = 34.2 Hz), 149.3, 141.4, 131.2, 127.4, 125.3, 124.3, 123.7, 121.6 (q, J_{C-F} = 275.1 Hz), 116.4, 111.3, 100.6 (q, J_{C-F} = 3.2 Hz), 49.9, 38.2, 31.0, 30.0, 25.9, 22.4, 14.2. ^{19}F NMR (471 MHz, DMSO-d_6): δ = −68.56 (s, 3F). HRMS: calcd. for $C_{20}H_{21}F_3N_6O^+$ ([M + H]$^+$): 419.18072, found: 419.17651.

10-((1-Decyl-1*H*-1,2,3-triazol-4-yl)methyl)-2-(trifluoromethyl)benzo[4,5]imidazo[1,2-*a*]pyrimidin-4(10*H*)-one (5q). Yellow solid, yield 73%, Mp 113–115 °C, TLC (cyclohexane/AcOEt, 6/4, *v*/*v*) R_f = 0.77. FTIR (ATR, cm^{-1}): 2994, 1687, 1598, 1567, 1492, 1476, 1278, 1136, 792, 744. ^{1}H NMR (500 MHz, DMSO-d_6): δ = 8.46 (dd, J = 8.1, 1.1 Hz, 1H), 8.11 (s, 1H), 7.73 (d, J = 8.0 Hz, 1H), 7.56 (td, J = 8.1, 1.1 Hz, 1H), 7.41 (td, J = 8.0, 1.1 Hz, 1H), 6.55 (s, 1H), 5.59 (s, 2H), 4.24 (t, J = 7.0 Hz, 2H), 1.68 (quint., J = 6.9 Hz, 2H), 1.37–0.96 (m, 14H), 0.82 (t, J = 7.0 Hz, 3H). ^{13}C NMR (126 MHz, DMSO-d_6): δ = 159.5, 151.5 (q, J_{C-F} = 34.6 Hz), 149.4, 141.3, 131.3, 127.6, 125.4, 124.3, 123.8, 120.7 (q, J_{C-F} = 275.1 Hz), 116.5, 111.2, 100.5 (q, J_{C-F} = 3.4 Hz), 50.1, 38.3, 31.5, 29.8, 29.0 (2C), 28.9, 28.6, 26.1, 22.3, 14.1. ^{19}F NMR (471 MHz, DMSO-d_6): δ = −68.59 (s, 3F). HRMS: calcd. For $C_{24}H_{29}F_3N_6O^+$ ([M + H]$^+$): 475.24332, found: 475.23892.

(2*S*,3*S*,4*R*,5*S*)-2-(Acetoxymethyl)-6-(4-((2-methyl-4-oxobenzo[4,5]imidazo[1,2-*a*]pyrimidin-10(4*H*)-yl)methyl)-1*H*-1,2,3-triazol-1-yl)tetrahydro-2*H*-pyran-3,4,5-triyl triacetate (5r). White solid, yield 73%, Mp 219–221 °C, TLC (100% AcOEt) R_f = 0.67/0.73. FTIR (ATR, cm^{-1}): 3114, 3071, 2954, 1748, 1732, 1686, 1586, 1536, 1474, 1420, 1365, 1235, 1222, 1208, 1034, 918, 763, 749. ^{1}H NMR (500 MHz, DMSO-d_6): δ = 8.43 (d, J = 8.0 Hz, 1H), 8.34 (s, 1H), 8.29 (d, J = 8.0 Hz, 0.20H), 8.35 (s, 0.20H),7.62 (d, J = 8.0 Hz, 0.20H), 7.53 (d, J = 8.0 Hz, 1H), 7.44 (t, J = 7.8 Hz, 1H), 7.38 (t, J = 7.1 Hz, 0.20H), 7.32 (t, J = 7.7 Hz, 1H), 7.26 (t, J = 7.5 Hz, 0.20H), 6.23 (d, J = 9.0 Hz, 1H), 5.95 (s, 1H), 5.87 (s, 0.20H), 5.66–5.59 (m, 0.40H), 5.56 (s, 2H), 5.51 (t, J = 9.3 Hz, 1H), 5.44 (t, J = 9.5 Hz, 1H), 5.10 (td, J = 9.7, 5.2 Hz, 1H), 4.28 (ddd, J = 10.3, 5.2, 2.7 Hz, 1H), 4.08–4.14 (m, 1H), 4.03–4.07 (m, 2H), 3.48–3.37 (m, 1H), 2.49 (s, 0.37H), 2.32 (s, 3H), 1.97 (s, 3H), 1.93 (s, 3H), 1.90 (s, 3H), 1.64 (s, 3H), 1.61 (s, 0.44H), 1.05 (s,

0.28H),1.03 (s, 0.35H), 1.02 (s, 0.25H)·^{13}C NMR (126 MHz, DMSO-d_6): δ = 170.4, 170.3, 170.0, 169.9, 169.8, 169.7, 168.8, 168.7, 164.8, 159.6, 158.8, 153.3, 148.8, 148.4, 143.3, 142.7, 141.9, 131.0, 130.0, 126.5, 125.7, 125.5, 123.4, 123.3, 122.9, 122.0, 118.2, 116.1, 115.2, 110.6, 101.4, 99.4, 84.6, 84.5, 74.0, 72.8, 72.7, 70.9, 70.8, 68.3, 62.3, 56.6, 42.2, 37.7, 24.6, 21.0, 20.9, 20.8, 20.6, 20.2, 19.2, 19.0. HRMS: calcd. for $C_{28}H_{30}N_6O_{10}^+$ ([M + H]$^+$): 611.21017, found: 661. 20 923.

(2*S*,3*R*,4*R*,5*S*)-2-(Acetoxymethyl)-6-(4-((2-methyl-4-oxobenzo[4,5]imidazo[1,2-*a*]pyrimidin-10(4*H*)-yl)methyl)-1*H*-1,2,3-triazol-1-yl)tetrahydro-2*H*-pyran-3,4,5-triyl triacetate (5s). Orange solid, yield 70%, Mp 105–107 °C TLC (100% AcOEt) R_f = 0.62/0.70. FTIR (ATR, cm^{-1}): 3078, 2957, 2854, 1746, 1676, 1598, 1580, 1475, 1455, 1270, 1042, 1024, 747. ^{1}H NMR (500 MHz, DMSO-d_6): δ = 8.41 (d, J = 8.1 Hz, 1H), 8.26 (d, J = 8.8 Hz, 0.60H), 8.22 (s, 1H), 8.21 (s, 0.36H), 7.60 (d, J = 8.0 Hz, 0.60H), 7.51 (d, J = 8.2 Hz, 1H), 7.43 (td, J = 8.1, 2.0 Hz, 1H), 7.36 (td, J = 8.8, 2.0 Hz, 0.60H), 7.31 (td, J = 8.2, 1.9 Hz, 1H), 7.24 (td, J = 8.0, 2.0 Hz, 0.60H), 6.08 (dd, J = 9.2, 0.9 Hz, 1H), 5.93 (s, 1H), 5.82 (s, 0.60H), 5.59 (s, 1H), 5.54 (s, 2H), 5.48 (d, J = 6.4 Hz, 0.60H), 5.45 (dd, J = 9.8, 6.4 Hz, 1H), 5.36 (dd, J = 3.6, 1.2 Hz, 1H), 5.34 (dd, J = 3.1, 1.2 Hz, 1H), 5.32 (dd, J = 3.1 Hz, 1.2, 0.60H), 4.50–4.41 (m, 1.60H), 4.07 (dd, J = 5.5, 1.9 Hz, 1H), 4.05 (dd, J = 5.5, 1.9 Hz, 1H), 3.99 (dd, J = 6.7, 3.1 Hz, 1H), 3.97 (dd, J = 6.7, 3.0 Hz, 0.60H), 2.50 (s, 1.60H), 2.30 (s, 3H), 2.09 (s, 3H), 2.08 (s, 1.60H), 1.90 (s, 3H), 1.89 (s, 1.60H), 1.87 (s, 3H), 1.86 (s, 1.60H), 1.62 (s, 1.60H), 1.60 (s, 3H). ^{13}C NMR (126 MHz, DMSO-d_6): δ = 170.4, 169.9, 169.0, 168.9, 165.1, 159.9, 158.9, 153.4, 148.8, 148.4, 143.0, 142.5, 141.9, 131.0, 129.9, 126.6, 125.8, 125.7, 123.6, 123.5, 123.0, 122.1, 118.1, 116.1, 115.2, 110.6, 101.4, 99.4, 85.2, 85.2, 73.8, 71.1, 71.1, 68.7, 68.6, 68.5, 68.0, 66.6, 63.4, 61.8, 59.8, 42.1, 37.6, 26.0, 24.9, 24.4, 23.0, 20.7, 20.6, 20.5, 20.1, 19.4, 19.3. HRMS: calcd. for $C_{28}H_{30}N_6O_{10}^+$ ([M + H]$^+$): 611.21017, found: 611.20483.

(2*S*,3*S*,4*S*)-2-(Acetoxymethyl)-5-(4-((2-methyl-4-oxobenzo[4,5]imidazo[1,2-*a*]pyrimidin-10(4*H*)-yl)methyl)-1*H*-1,2,3-triazol-1-yl)tetrahydrofuran-3,4-diyl diacetate (5t). Orange viscous oil, yield 77%, TLC (100% AcOEt) R_f = 0.5/0.62. FTIR (ATR, cm^{-1}): 3082, 2955, 2858, 1744, 1678, 1598, 1580, 1477, 1453, 1270, 1040, 1024, 749. ^{1}H NMR (500 MHz, DMSO-d_6): δ = 8.41 (d, J = 8.1 Hz, 1H), 8.26 (d, J = 8.1 Hz, 0.3H), 8.24 (s, 0.3H), 8.21 (s, 1H), 7.59 (d, J = 8.2 Hz, 2H), 7.44 (td, J = 7.8 Hz, 1H), 7.37 (td, J = 7.7 Hz, 0.3H), 7.31 (td, J = 7.8 Hz, 1H), 7.24 (td, J = 7.7 Hz, 0.2H), 6.22 (d, J = 3.7 Hz, 0.3H), 6.21 (d, J = 3.7 Hz, 1H), 5.93 (s, 1H), 5.82 (s, 0.5H), 5.70 (q, J = 5.6 Hz, 1H), 5.59 (s, 1H), 5.55 (s, 2H), 5.45 (q, J = 5.6 Hz, 1H), 4.36 (q, J = 4.6 Hz, 1.6H), 4.23 (dd, J = 12.3, 3.7 Hz, 1.7H), 4.04 (dd, J = 12.3, 4.8 Hz, 1.7H), 2.54 (s, 2H), 2.29 (s, 3H), 2.00 (d, J = 5.2 Hz, 6H), 1.87 (s, 3H), 1.84 (s, 0.4H), 1.82 (s, 1H), 1.80 (s, 3H). ^{13}C NMR (126 MHz, DMSO-d_6): δ = 172.4, 170.5, 170.4, 170.0, 169.7, 165.1, 159.9, 158.9, 153.5, 148.8, 148.3, 142.9, 142.5, 141.9, 131.1, 129.9, 126.7, 125.7, 124.2, 124.1, 123.7, 123.0, 122.2, 118.2, 116.2, 115.2, 110.6, 101.4, 99.4, 92.6, 90.0, 82.9, 80.7, 80.5, 74.0, 73.4, 73.1, 71.4, 70.9, 63.5, 63.0, 61.3, 42.1, 37.6, 24.4, 21.3, 20.9, 20.6, 20.5, 20.4, 19.4. HRMS: calcd. for $C_{25}H_{26}N_6O_8^+$ ([M + H]$^+$): 539.18904, found: 539.18414.

2-Methyl-10-((1-phenyl-1*H*-1,2,3-triazol-4-yl)methyl)benzo[4,5]imidazo[1,2-*a*]pyrimidin-4(10*H*)-one (5u). White solid, yield 65%, Mp 195–197 °C, TLC (100% AcOEt) R_f = 0.64/0.78. FTIR (ATR, cm^{-1}): 3081, 2918, 1675, 1583, 1538, 1473, 1415, 1275, 1163, 807, 761, 741, 691. ^{1}H NMR (500 MHz, DMSO-d_6): δ = 8.77 (s, 1H), 8.43 (d, J = 8.0 Hz, 2H), 7.79 (dd, J = 8.7, 1.2 Hz, 2H), 7.65 (dd, J = 11.8, 8.1 Hz, 2H), 7.60–7.56 (m, 3H), 7.52–7.50 (m, 3H), 7.41 (td, J = 7.1, 1.1 Hz, 1H), 7.41 (tt, J = 8.0, 1.7 Hz, 1H), 7.35 (dd, J = 8.2, 1.1 Hz, 1H), 7.32 (dd, J = 8.1, 1.1 Hz, 1H), 5.98 (s, d, J = 0.7 Hz, 1H), 5.98 (s, d, J = 0.7 Hz, 1H), 5.64 (s, 2H), 5.61 (s, 2H), 2.31 (d, J = 0.7 Hz, 3H), 2.30 (d, J = 0.7 Hz, 3H). ^{13}C NMR (126 MHz, DMSO-d_6): δ = 164.9, 164.8, 159.7, 159.6, 148.8, 148.7, 146.6, 143.3, 137.1, 137.0, 131.2, 131.0, 130.8, 130.4 (2C), 130.1 (2C), 129.3, 126.8 (2C), 126.7, 126.6, 125.6, 125.5, 123.0, 123.0, 122.4, 120.6 (2C), 116.1, 111.1, 110.8, 101.5, 101.4, 85.9 (2C), 38.4, 37.7, 24.7, 24.6. HRMS: calcd. for $C_{20}H_{16}N_6O^+$ ([M + H]$^+$): 357.14638, found: 357.14319.

2-Methyl-10-((1-(*p*-tolyl)-1*H*-1,2,3-triazol-4-yl)methyl)benzo[4,5]imidazo[1,2-*a*]pyrimidin-4(10*H*)-one (5v). White solid, yield 70%, Mp 247–249 °C, TLC (100% AcOEt) R_f = 0.8/0.87. FTIR (ATR, cm^{-1}): 3074, 2918, 2857, 1679, 1583, 1546, 1476, 1421, 1278, 809, 766, 751. ^{1}H NMR (500 MHz, DMSO-d_6): δ = 8.55 (s, 2H), 8.42 (d, J = 8.2 Hz, 1H), 8.27 (d, J = 8.2 Hz, 0.5H), 7.62 (d, J = 8.8 Hz, 1H), 7.60 (d, J = 8.5 Hz, 4H), 7.45 (td, J = 8.2, 1.2 Hz, 0.7H), 7.36 (td, J = 8.2, 1.6 Hz, 1H), 7.33 (td, J = 8.8, 1.6 Hz, 1H), 7.29 (d, J = 8.5 Hz, 4H), 7.24 (td, J = 8.8, 1.6 Hz, 1H), 5.94 (s, 0.6H), 5.84 (s, 1H), 5.66 (s, 2H), 5.61 (s, 1H), 2.57 (s, 6H), 2.30 (s, 6H). ^{13}C NMR (126 MHz, DMSO-d_6): δ = 165.1, 159.9, 158.9, 153.5, 148.9, 148.4, 143.4, 142.9, 141.9, 139.2, 134.8, 131.1, 130.7 (2C), 130.6 (2C), 129.9, 126.6, 125.7, 125.6, 123.0, 122.4, 122.3, 122.1, 120.8 (2C), 120.7 (2C), 118.2, 116.2, 115.2, 110.7, 101.4, 99.4, 42.3, 37.7, 24.5, 20.9, 19.4. HRMS: calcd. for $C_{21}H_{18}N_6O^+$ ([M + H]$^+$): 371.16203, found: 371.15881.

4-(4-((2-Methyl-4-oxobenzo[4,5]imidazo[1,2-*a*]pyrimidin-10(4*H*)-yl)methyl)-1*H*-1,2,3-triazol-1-yl)benzonitrile (5w). White solid, yield 68%, Mp 263–265 °C, TLC (100% AcOEt) R_f = 0.52/0.54. FTIR (ATR, cm^{-1}): 3084, 2926, 2873, 1673, 1579, 1550, 1474, 1419, 1275, 802, 763. ^{1}H NMR (500 MHz, DMSO-d_6): δ = 8.74 (s, 2H), 8.42 (d, J = 8.8 Hz, 1H), 8.26 (d, J = 8.1 Hz, 0.5H), 7.99 (d, J = 5.2 Hz, 1H), 7.97 (d, J = 4.5 Hz, 2H), 7.93 (d, J = 4.5 Hz, 2H), 7.92 (d, J = 5.2 Hz, 1H), 7.62 (d, J = 7.6 Hz, 1H), 7.59 (d, J = 8.1 Hz, 0.5H), 7.45 (td, J = 8.8, 1.6 Hz, 1H), 7.36 (td, J = 8.1, 1.6 Hz, 0.3H), 7.32 (td, J = 7.6, 1.6 Hz, 1H), 7.24 (td, J = 7.6, 1.6 Hz, 0.3H), 5.94 (s, 1H), 5.85 (s, 0.5H), 5.68 (s, 1H), 5.63 (s, 2H), 2.56 (s, 2H), 2.31 (s, 3H). ^{13}C NMR (126 MHz, DMSO-d_6): δ = 165.1, 159.9, 158.9, 153.4, 148.9, 148.4, 144.1, 143.6, 141.9, 140.0, 139.9, 134.6 (2C), 134.5 (2C), 131.1, 123.0, 126.7, 125.7, 125.6, 123.0, 122.8, 122.7, 122.1, 121.4 (2C), 121.3 (2C), 118.5, 118.2, 116.2, 115.2, 111.9, 111.9, 110.6, 101.5, 99.5, 42.2, 37.7, 24.5, 19.40. HRMS: calcd. For $C_{21}H_{15}N_7O^+$ ([M + H]$^+$): 382.14163, found: 382.13846.

10-((1-Benzyl-1*H*-1,2,3-triazol-4-yl)methyl)-2-methylbenzo[4,5]imidazo[1,2-*a*]pyrimidin-4(10*H*)-one (5x). White solid, yield 64%, Mp 223–225 °C, TLC (100% AcOEt) R_f = 0.40/0.42. FTIR (ATR, cm^{-1}): 3082, 2953, 2853, 1675, 1595, 1577, 1472, 1454, 1267, 745, 735, 696. ^{1}H NMR (500 MHz, DMSO-d_6): δ = 8.40 (d, J

= 8.1 Hz, 1H), 8.26 (d, J = 6.8 Hz, 0.05H), 8.07 (s, 0.20H), 8.05 (s, 1H), 7.58 (d, J = 8.1 Hz, 0.02H), 7.55 (d, J = 8.2 Hz, 1H), 7.43 (td, J = 7.8, 1.2 Hz, 1H), 7.36 (td, J = 7.8, 1.2 Hz, 0.22H), 7.30 (td, J = 7.1, 1.4 Hz, 1H), 7.33–7.28 (m, 3H), 7.25–7.23 (m, 0.7H), 7.21 (dd, J = 7.6, 2.0 Hz, 0.3H),7.19 (dd, J = 7.6, 2.0 Hz, 2H), 5.92 (s, 1H), 5.81 (s, 0.2H), 5.56 (s, 0.5H), 5.51 (s, 2H), 5.47 (s, 2H), 2.52 (s, 1H), 2.28 (s, 3H). ^{13}C NMR (126 MHz, DMSO-d_6): δ = 165.0, 159.9, 158.9, 153.6, 148.8, 148.3, 142.6, 142.1, 141.9, 136.1, 136.1, 131.1, 129.9, 129.2 (2C), 128.7 (2C), 128.4 (2C), 128.3 (2C), 126.6, 125.6, 124.4, 124.4, 122.9, 122.1, 118.1, 116.1, 115.2, 110.6, 101.3, 99.3, 53.6, 42.3, 37.8, 24.4, 19.4. HRMS: calcd. for $C_{21}H_{18}N_6O^+$([M + H]$^+$): 371.16203, found: 371.15796.

Data availability

All data have been provided in the main article.

Author contributions

Chaimae Hourma: organic synthesis, characterization and catalytic experiments; Mohamed Belhajja: catalyst synthesis and characterization; Mohsine Driowya: formal analysis, investigation, and writing the original draft; Hamza Tachallait: characterization and writing – review; Rachid Benhida: design and review & editing; Khalid Bougrin: conceptualization, funding acquisition and writing – review. All the authors discussed the results and reviewed the manuscript.

Conflicts of interest

There are no conflicts to declare.

Acknowledgements

This work was supported by UM5R and UM6P. The authors would like to acknowledge the CNRST Morocco for spectral analysis and the PhD grant to C. Hourma awarded under the Excellence Research Fellowship program (edition 2021).

References

1 L. Song, Y. Lai, H. Li, J. Ding, H. Yao, Q. Su, B. Huang, M. A. Ouyang and R. Tong, *J. Org.Chem.*, 2022, **87**, 10550–10554, DOI: 10.1021/acs.joc.2c01391.

2 C. Castiello, P. Junghanns, A. Mergel, C. Jacob, C. Ducho, S. Valente, D. Rotili, R. Fioravanti, C. Zwerge and A. Mai, *Green Chem.*, 2023, **25**, 2109–2169, DOI: 10.1039/D2GC03772F.

3 K. S. Kumar, A. R. Robert, N. Kerru and S. Maddila, *Results Chem.*, 2023, **5**, 100692–100697, DOI: 10.1016/j.rechem.2022.100692.

4 S. Alvi, V. Jayant and R. Ali, *ChemistrySelect*, 2022, **7**, e202200704, DOI: 10.1002/slct.202200704.

5 T. Sahoo, J. Panda, J. Sahu, D. Sarangi, S. K. Sahoo, B. B. Nanda and R. Sahu, *Curr. Org. Synth.*, 2020, **17**, 426–439, DOI: 10.2174/1570179417666200506102535.

6 S. Santos, D. Raydan, J. C. Cunha, N. Viduedo, A. M. Silva and M. M. B. Marques, *Catalysts*, 2021, **11**, 1108–1128, DOI: 10.1039/D3OB00277B.

7 C. G. Avila-Ortiz and E. Juaristi, *Molecules*, 2020, **25**, 3579–3592, DOI: 10.3390/molecules25163579.

8 M. Miceli, P. Frontera, A. Macario and A. Malara, *Catalysts*, 2021, **11**, 591–607, DOI: 10.3390/catal11050591.

9 H. U. Blaser, A. Indolese, A. Schnyder, H. Steiner and M. Studer, *J. Mol. Catal. A Chem.*, 2001, **173**, 3–18, DOI: 10.1016/S1381-1169(01)00143-1.

10 G. Gao, J. Q. Di, H. Y. Zhang, L. P. Mo and Z. H. Zhang, *J. Catal.*, 2020, **387**, 39–46, DOI: 10.1016/j.jcat.2020.04.013.

11 G. Latha, N. Devarajan and P. Suresh, *ChemistrySelect*, 2020, **5**, 10041–10047, DOI: 10.1002/slct.202002661.

12 A. Dhakshinamoorthy and H. Garcia, *Chem. Soc. Rev.*, 2014, **43**, 5750–5765, DOI: 10.1039/C3CS60442J.

13 S. Perrone, L. Troisi and A. Salomone, *Eur. J. Org. Chem.*, 2019, **29**, 4626–4643, DOI: 10.1039/C3CS60442J.

14 P. K. Baroliya, J. Chopra, T. Pal, S. Maiti, S. A. Al-Thabaiti, M. Mokhtar and D. Maiti, *ChemCatChem*, 2021, **13**, 4655–4678, DOI: 10.1002/cctc.202100755.

15 S. Adeyeye Nafiu, A. M. Ajeebi, H. S. Alghamdi, M. A. Aziz and M. Nasiruzzaman Shaikh, *Asian J. Org. Chem.*, 2023, **12**, e202300051, DOI: 10.1002/ajoc.202300051.

16 M. L. Richards and P. J. Scott, in *Green Techniques for Organic Synthesis and Medicinal Chemistry*, ed. W. Zhang and B. W. Cue, John Wiley & Sons, Ltd, New Jersey, 2012, ch. 3, pp. 33–66, DOI: 10.1002/9780470711828.ch3.

17 (*a*) S. Saneinezhad, L. Mohammadi, V. Zadsirjan, F. F. Bamoharram and M. M. Heravi, *Sci. Rep.*, 2020, **10**, 14540–14554, DOI: 10.1038/s41598-024-57682-y; (*b*) M. Nasrollahzadeh, F. Soleimani, Z. Nezafat, Y. Orooji and F. Ahmadpoor, *Biomass Convers. Biorefin.*, 2021, 1–15, DOI: 10.1007/s13399-021-02005-8.

18 T. Philibert, B. H. Lee and N. Fabien, *Appl. Biochem. Biotechnol.*, 2017, **181**, 1314–1337, DOI: 10.1007/s12010-016-2286-2.

19 T. Muthukumar, G. Sreekumar, T. P. Sastry and M. Chamundeeswari, *Rev. Adv. Mater. Sci.*, 2018, **53**, 29–39, DOI: 10.1515/rams-2018-0002.

20 D. Klemm, B. Heublein, H. P. Fink and A. Bohn, *Angew. Chem., Int. Ed.*, 2005, **44**, 3358–3393, DOI: 10.1002/anie.200460587.

21 M. Sadeghi, *RSC Adv.*, 2024, **14**, 12676–12702, DOI: 10.1039/D4RA00775A.

22 K. Ghai, A. K. Gupta and P. K. Gupta, *J. Biol. Act. Prod. Nat.*, 2012, **2**, 250–255, DOI: 10.1080/22311866.2012.10719132.

23 M. Tanase-Opedal, E. Espinosa, A. Rodríguez and G. Chinga-Carrasco, *Materials*, 2019, **12**, 3006–3020, DOI: 10.48442/IMIST.PRSM/jasi-v8i1-3.23321.

24 M. A. Abourehab, R. R. Rajendran, A. Singh, S. Pramanik, P. Shrivastav, M. J. Ansari, R. Manne, L. S. Amaral and A. Deepak, *Int. J. Mol. Sci.*, 2022, **23**, 9035–9091, DOI: 10.3390/ijms23169035.

25 (*a*) L. Bahsis, E. H. Ablouh, M. E. Hachim, H. Anane, M. Taourirte, M. Julve and S. E. Stiriba, *Appl. Organomet. Chem.*, 2021, **35**, e6275, DOI: 10.1002/aoc.6275; (*b*)

R. N. Baig and R. S. Varma, *Green Chem.*, 2013, 1839–1843, DOI: 10.1039/C3GC40401C; (*c*) A. Pourjavadi, A. Motamedi, S. H. Hosseini and M. Nazari, *RSC Adv.*, 2016, **6**, 19128–19135, DOI: 10.1039/C5RA25519H; (*d*) L. Bahsis, E. H. Ablouh, H. Anane, M. Taourirte, M. Julve and S. E. Stiriba, *RSC Adv.*, 2020, **10**, 32821–32832, DOI: 10.1039/D0RA06410F; (*e*) S. Sabaqian, F. Nemati, M. M. Heravi and H. T. Nahzomi, *Appl. Organomet. Chem.*, 2017, **31**, e3660, DOI: 10.1002/aoc.3660; (*f*) E. Doustkhah, M. Heidarizadeh, S. Rostamnia, A. Hassankhani, B. Kazemi and X. Liu, *Mater. Lett.*, 2018, **216**, 139–143, DOI: 10.1016/j.matlet.2018.01.014.

26 (*a*) A. Maleki, H. Movahed and R. Paydar, *RSC Adv.*, 2016, **6**, 13657–13665, DOI: 10.1039/C5RA21350A; (*b*) A. Maleki, P. Ravaghi, M. Aghaei and H. Movahed, *Res. Chem. Intermed.*, 2017, **43**, 5485–5494, DOI: 10.1007/s11164-017-2941-4.

27 A. Ali, S. Ambreen, Q. Maqbool, S. Naz, M. F. Shams, M. Ahmad, A. R. Phull and M. Zia, *J. Phys. Chem. Solids*, 2016, **98**, 174–182, DOI: 10.1016/j.jpcs.2016.07.007.

28 S. Gao, Y. Shi, S. Zhang, K. Jiang, S. Yang, Z. Li and E. Takayama-Muromachi, *J. Phys. Chem.*, 2008, **112**, 10398–10401, DOI: 10.1021/jp802500a.

29 (*a*) M. Dinodia, *Mini-Rev. Org. Chem.*, 2023, **20**, 735–747, DOI: 10.2174/1570193X19666211231101747; (*b*) A. El Mahmoudi, R. Fegrouche, H. Tachallait, J. P. Lumaret, S. Arshad, K. Karrouchi and K. Bougrin, *Pest Manage. Sci.*, 2023, **79**, 4847–4857, DOI: 10.1002/ps.7686; (*c*) A. El Mahmoudi, A. S. Tareau, M. Barreau, S. Chevalier, C. Hourma, L. Demange, R. Benhida and K. Bougrin, *Bioorg. Med. Chem. Lett.*, 2023, **96**, 129517–129524, DOI: 10.1016/j.bmcl.2023.129517; (*d*) M. Driowya, A. Saber, H. Marzag, L. Demange, R. Benhida and K. Bougrin, *Molecules*, 2016, **21**, 492–547, DOI: 10.3390/molecules21040492.

30 (*a*) S. Rani, S. Teotia and S. Nain, *Pharm. Chem. J.*, 2024, **57**, 1909–1917, DOI: 10.1007/s11094-024-03096-z; (*b*) G. Tian, Q. Song, Z. Liu, J. Guo, S. Cao and S. Long, *Eur. J. Med. Chem.*, 2023, **259**, 115603–115627, DOI: 10.1039/D2BM01698B; (*c*) P. Bansode, D. Pore, S. Tayade, S. Patil, P. Choudhari and G. Rashinkar, *Results Chem.*, 2023, **5**, 100758–100772, DOI: 10.1016/j.rechem.2022.100758; (*d*) I. S. A. Nasr, W. S. Koko, T. A. Khan, R. Schobert and B. Biersack, *Biomedicines*, 2023, **11**, 219–229, DOI: 10.3390/biomedicines11010219; (*e*) A. O. Abdelhamid, S. M. El-Enany and W. A. Gomha, *J. Heterocycl. Chem.*, 2019, **56**, 2487–2493, DOI: 10.1002/jhet.3638; (*f*) C. G. Neochoritis, T. Zarganes-Tzitzikas, C. A. Tsoleridis, J. Stephanidou-Stephanatou, C. A. Kontogiorgis, D. J. Hadjipavlou-Litina and T. Choli-Papadopoulou, *Eur. J. Med. Chem.*, 2011, **46**, 297–306, DOI: 10.1016/j.ejmech.2010.11.018.

31 K. B. Puttaraju, K. Shivashankar, M. Mahendra, V. P. Rasal, P. N. V. Vivek, K. Rai and M. B. Chanu, *Eur. J. Med. Chem.*, 2013, **69**, 316–322, DOI: 10.1016/j.ejmech.2013.07.015.

32 S. Khan, M. Kale, F. Siddiqui and N. Nema, *Digit. Chin. Med.*, 2021, **4**, 102–119, DOI: 10.1016/j.dcmed.2021.06.004.

33 D. I. Othman, A. Hamdi, S. S. Tawfik, A. A. Elgazar and A. S. Mostafa, *J. Enzyme Inhib. Med. Chem.*, 2023, **38**, 2166037–2166054, DOI: 10.1080/14756366.2023.2166037.

34 N. Asemanipoor, M. Mohammadi-Khanaposhtani, S. Moradi, M. Vahidi, M. Asadi, M. A. Faramarzi, M. Mahdavi, M. Biglar, B. Larijani, H. Hamedifar and M. H. Hajimiri, *Bioorg. Chem.*, 2020, **95**, 103482–103490, DOI: 10.1016/j.bioorg.2019.103482.

35 (*a*) M. S. Singh, S. Chowdhury and S. Koley, *Tetrahedron*, 2016, **72**, 5257–5283; (*b*) J. E. Hein and V. V. Fokin, *Chem. Soc. Rev.*, 2010, **39**, 1302–1315, DOI: 10.1039/B904091A.

36 (*a*) M. Breugst and H. U. Reissig, *Angew. Chem., Int. Ed.*, 2020, **59**, 12293–12307; (*b*) C. Wang, D. Ikhlef, S. Kahlal, J. Y. Saillard and D. Astruc, *Coord. Chem. Rev.*, 2016, **316**, 1–20, DOI: 10.1016/j.ccr.2016.02.010.

37 (*a*) V. V. Rostovtsev, L. G. Green, V. V. Fokin and K. B. Sharpless, *Angew. Chem., Int.*, 2002, **41**, 2596–2599, DOI: 10.1002/1521-3773(20020715)41:14<2596::AID-ANIE2596>3.0.CO;2-4; (*b*) C. W. Tornoe, C. Christensen and M. J. Meldal, *J. Org. Chem.*, 2002, **67**, 3057–3064, DOI: 10.1021/jo011148j.

38 A. Amiri, S. Abedanzadeh, B. Davaeil, S. M. Asghari, A. Shaabani and A. A. Moosavi Movahedi, *Sci. Cultiv.*, 2022, **13**, 70–76, https://www.sciencecultivation.ir/article_701314.html?lang=en.

39 I. V. Gürsel, T. Noël, Q. Wang and V. Hessel, *Green Chem.*, 2015, **17**, 2012–2026, DOI: 10.1039/C4GC02160F.

40 S. Noriega, E. Leyva, E. Moctezuma, L. Flores and S. Loredo-Carrillo, *Curr. Org. Chem.*, 2020, **24**, 536–549, DOI: 10.2174/1385272824666200226120135.

41 (*a*) S. Zhang and L. Zhao, *Nat. Commun.*, 2019, **10**, 4848–4857, DOI: 10.1038/s41467-019-12889-w; (*b*) F. Sączewski, E. Dziemidowicz-Borys, P. J. Bednarski, R. Grünert, M. Gdaniec and P. Tabin, *J. Inorg. Biochem.*, 2006, **100**, 1389–1398, DOI: 10.1016/j.jinorgbio.2006.04.002; (*c*) H. Struthers, T. L. Mindt and R. Schibli, *Dalton Trans.*, 2010, **39**, 675–696, DOI: 10.1039/B912608B.

42 S. Chassaing, V. Bénéteau and P. J. C. S. Pale, *Catal. Sci. Technol.*, 2016, **6**, 923–957, DOI: 10.1039/C5CY01847A.

43 P. Shiri and J. Aboonajmi, *Beilstein J. Org. Chem.*, 2020, **16**, 551–586, DOI: 10.3762/bjoc.16.52.

44 M. Miceli, P. Frontera, A. Macario and A. Malara, *Catalysts*, 2021, **11**, 591–607, DOI: 10.3390/catal11050591.

45 (*a*) R. N. Baig and R. S. Varma, *Green Chem.*, 2013, **15**, 398–417, DOI: 10.1039/C2GC36455G; (*b*) V. Dorostian, B. Maleki, S. Peiman and M. Ghani, *Sci. Rep.*, 2025, **15**, 10571–10589, DOI: 10.1038/s41598-025-94548-3; (*c*) V. Vikhe, D. Aute, V. Kadnor, G. Shirole, B. Uphade and A. Gadhave, *Polycyclic Aromat. Compd.*, 2025, **45**, 322–341, DOI: 10.1080/10406638.2024.2405527; (*d*) S. Peiman and B. Maleki, *Sci. Rep.*, 2024, **14**, 17401–17422, DOI: 10.1038/s41598-024-75629-1.

46 R. K. Donato and A. Mija, *Polymers*, 2019, **12**, 32–95, DOI: 10.3390/polym12010032.

47 M. Belhajja, M. Driowya, O. Cherkaoui and K. Bougrin, *J. Clean. Prod.*, 2024, **485**, 144389–144414, DOI: 10.1016/j.jclepro.2024.144389.

48 L. Wang, Y. Shang, J. Zhang, J. Yuan and J. Shen, *Adv. Colloid Interface Sci.*, 2023, **321**, 103012–103022, DOI: 10.1016/j.cis.2023.103012.
49 V. Hessel, N. N. Tran, M. R. Asrami, Q. D. Tran, N. V. D. Long, M. Escribà-Gelonch, J. Osorio Tejada and S. L. K. Sundmacher, *Green Chem.*, 2022, **24**, 410–437, DOI: 10.1039/D1GC03662A.
50 M. O. Sydnes, *Curr. Green Chem.*, 2018, **5**, 22–39, DOI: 10.2174/2213346105666180222122637.
51 R. N. Yadav, A. K. Srivastava and B. K. Banik in *Green Approaches in Medicinal Chemistry for Sustainable Drug Design*, ed. B. K. Banik, Elsevier Inc., Amsterdam, 2020, ch. 10, pp. 353–425, DOI: 10.1016/B978-0-12-817592-7.00010-1.
52 M. O. Sydnes, *Curr. Green Chem.*, 2014, **1**, 216–226, DOI: 10.2174/2213346101666140221225404.
53 J. Behal, M. S. Maru, R. Katwal, D. Pathak and V. Kumar, *J. Alloys Compd. Commun.*, 2024, **3**, 100013–100024, DOI: 10.1016/j.jacomc.2024.100013.
54 S. Puri, B. Kaur, A. Parmar and H. Kumar, *Curr. Org. Chem.*, 2013, **17**, 1790–1828, DOI: 10.2174/13852728113179990018.
55 (*a*) R. Taheri-Ledari, J. Rahimi and A. Maleki, *Ultrason. Sonochem.*, 2019, **59**, 104737–104745, DOI: 10.1016/j.ultsonch.2019.104737; (*b*) B. Maleki, M. Baghayeri, S. A. J. Abadi, R. Tayebee and A. Khojastehnezhad, *RSC Adv.*, 2016, **6**, 96644–96661, DOI: 10.1039/C6RA20895A; (*c*) J. Safari and L. Javadian, *Ultrason. Sonochem.*, 2015, **22**, 341–348, DOI: 10.1016/j.ultsonch.2014.02.002.
56 (*a*) S. Alaoui, M. Driowya, L. Demange, R. Benhida and K. Bougrin, *Ultrason. Sonochem.*, 2018, **40**, 289–297, DOI: 10.1016/j.ultsonch.2017.07.019; (*b*) F. Z. Thari, H. Tachallait, N. E. El Alaoui, A. Talha, S. Arshad, E. Álvarez, K. Karrouchi and K. Bougrin, *Ultrason. Sonochem.*, 2020, **68**, 105222–105232, DOI: 10.1016/j.ultsonch.2020.105222; (*c*) A. Talha, C. Favreau, M. Bourgoin, G. Robert, P. Auberger, L. E. Ammari, M. Saadi, R. Benhida, A. R. Martin and K. Bougrin, *Ultrason. Sonochem.*, 2021, **78**, 105748–105759, DOI: 10.1016/j.ultsonch.2021.105748; (*d*) A. EL Mahmoudi, H. Tachallait, Z. Moutaoukil, S. Arshad, K. Karrouchi, R. Benhida and K. Bougrin, *Chem. Select.*, 2022, **7**, e202203072, DOI: 10.1002/slct.202203072.
57 L. Mokhi, A. Moussadik, M. Driowya, A. El Mahmoudi, H. Tachallait, R. Benhida, A. El Hamidi and K. Bougrin, *J. Mol. Liq.*, 2024, **395**, 123763–123779, DOI: 10.1016/j.molliq.2023.123763.
58 A. Talha, A. Mourhly, H. Tachallait, M. Driowya, A. El Hamidi, S. Arshad, K. Karrouch, S. Arsalane and K. Bougrin, *Tetrahedron*, 2021, **90**, 132215–132227, DOI: 10.1016/j.tet.2021.13221.
59 Z. Cheng, X. Chen, D. Zhai, F. Gao, T. Guo, W. Li, S. Hao, J. Ji and B. Wang, *J. Nanobiotechnol.*, 2018, **16**, 24–36, DOI: 10.1186/s12951-018-0353-2.
60 X. Zhang, Y. Guo, W. Li, J. Zhang, H. Wu, N. Mao and H. Zhang, *Nanomaterials*, 2021, **11**, 1068–1091, DOI: 10.3390/nano11051068.
61 S. Liu, B. Yu, S. Wang, Y. Shen and H. Cong, *Adv. Colloid Interface Sci.*, 2020, **281**, 102165–102194, DOI: 10.1016/j.cis.2020.102165.
62 T. Nikiforova, V. Kozlov and M. Islyaikin, *J. Environ. Chem. Eng.*, 2019, **7**, 103417–103428, DOI: 10.1016/j.jece.2019.103417.
63 T. Rajh, L. X. Chen, K. Lukas, T. Liu, M. C. Thurnauer and D. M. Tiede, *J. Phys. Chem. B*, 2002, **106**, 10543–10552, DOI: 10.1021/jp021235v.
64 S. Saleem, M. Irfan, M. Y. Naz, S. Shukrullah, M. A. Munir, M. Ayyaz, A. S. Alwadie, S. Legutko, J. Petrů and S. Rahman, *Materials*, 2022, **15**, 3502–3515, DOI: 10.3390/ma15103502.
65 A. M. Predescu, R. Vidu, P. Vizureanu, A. Predescu, E. Matei and C. Predescu, *Materials*, 2020, **13**, 3086–3099, DOI: 10.3390/ma13143086.
66 P. S. Anbinder, C. Macchi, J. Amalvy and A. Somoza, *Carbohydr. Polym.*, 2019, **222**, 114987–114993, DOI: 10.1016/j.carbpol.2019.114987.
67 T. Wang, W. Yang, T. Song, C. Li, L. Zhang, H. Wang and L. Chai, *RSC Adv.*, 2015, **5**, 50011–50018, DOI: 10.1039/C5RA03951G.
68 B. Ma, Q. Sun, J. Yang, J. Wizi, X. Hou and Y. Yang, *Environ. Sci. Pollut. Res.*, 2017, **24**, 17711–17718, DOI: 10.1007/s11356-017-9410-x.
69 S. Sharma, A. Gupta, A. Kumar, C. G. Kee, H. Kamyab and S. M. Saufi, *Clean Technol. Environ. Policy*, 2018, **20**, 2157–2167, DOI: 10.1007/s10098-018-1498-2.
70 W. Zhao, R. Yang, Y. Zhang and L. Wu, *Green Chem.*, 2012, **14**, 3352–3360, DOI: 10.1039/C2GC36243K.
71 (*a*) H. E. Hashem, E. A. Mohamed, A. A Farag, N. A. Negm and E. A. Azmy, *Appl. Organomet. Chem.*, 2021, **35**, e6322, DOI: 10.1002/aoc.6322; (*b*) A. Aluigi, C. Tonetti, C. Vineis, C. Tonin and G. Mazzuchetti, *Eur. Polym. J.*, 2011, **47**, 1756–1764, DOI: 10.1016/j.eurpolymj.2011.06.009.
72 B. Fernández-d'Arlas, *Sci. Rep.*, 2019, **9**, 14810–14821, DOI: 10.1038/s41598-019-51393-5.
73 B. Fernández-d'Arlas, *Eur. Polym. J.*, 2018, **103**, 187–197, DOI: 10.1016/j.eurpolymj.2018.04.010.
74 Z. Jiang, W. Li, Y. Wang and Q. Wang, *AATCC J. Res.*, 2022, 43–48, DOI: 10.1177/23305517211060778.
75 Z. Dong, D. Wang, X. Liu, X. Pei, L. Chen and J. Jin, *J. Mater. Chem. A*, 2014, **2**, 5034–5040, DOI: 10.1039/C3TA14751G.
76 Q. Ai, Z. Yuan, R. Huang, C. Yang, G. Jiang, J. Xiong, Z. Huang and S. Yuan, *J. Mater. Sci.*, 2019, **54**, 4212–4224, DOI: 10.1007/s10853-018-3141-3.
77 S. Alahyaribeik and A. Ullah, *Int. J. Biol. Macromol.*, 2020, **148**, 449–456, DOI: 10.1016/j.ijbiomac.2020.01.144.
78 L. Perreux and A. Loupy, *Tetrahedron*, 2001, **57**, 9199–9223, DOI: 10.1016/S0040-4020(01)00905-X.
79 M. Baghbanzadeh and C. O. Kappe, *Aust. J. Chem.*, 2009, **62**, 244–249, DOI: 10.1071/CH08450.
80 S. M. Sirko, N. Y. Gorobets, V. I. Musatov and S. M. Desenko, *Molecules*, 2009, **14**, 5223–5234, DOI: 10.3390/molecules14125223.

81 S. Balalaie, M. M. Hashemi and M. Akhbari, *Tetrahedron Lett.*, 2003, **44**, 1709–1711, DOI: **10.1016/S0040-4039(03)00018-2**.
82 A. V. Pandit, V. P. Sarvothaman and V. V. Ranade, *Ultrason. Sonochem.*, 2021, **77**, 105677–105693, DOI: **10.1016/j.ultsonch.2021.105677**.
83 A. M. Pavlenko and H. Koshlak, *Energies*, 2021, **14**, 7996–8014, DOI: **10.3390/en14237996**.
84 E. N. Ulomskiy, O. S. El'tsov, S. S. Borisov, K. V. Savateev, E. K. Voinkov, V. V. Fedotov and V. L. Rusinov, *Chem. Heterocycl. Compd.*, 2014, **50**, 1005–1013, DOI: **10.1007/s10593-014-1556-6**.
85 L. Perreux, A. Loupy and F. Volatron, *Tetrahedron*, 2002, **58**, 2155–2162, DOI: **10.1016/S0040-4020(02)00085-6**.
86 M. Miceli, P. Frontera, A. Macario and A. Malara, *Catalysts*, 2021, **11**, 591–607, DOI: **10.3390/catal11050591**.
87 P. Knepper, *TrAC*, 2003, **22**, 708–724, DOI: **10.1016/S0165-9936(03)01008-2**.
88 C. I. Nieto, P. Cabildo, M. Á. García, R. M. Claramunt, I. Alkorta and J. Elguero, *Beilstein J. Org. Chem.*, 2014, **10**, 1620–1629, DOI: **10.3762/bjoc.10.168**.